ESA contract
Martian Environmental Model

Ref : ESA 11369/95/NL/JG(SC)

WP6 deliverable :

Updated Detailed Design Document for the Martian Atmospheric General Circulation Model

François Forget, Frédéric Hourdin, Richard Fournier, Matthew Collins,
Christophe Hourdin, Steven Lewis
LMD/AOPP

November 9, 1999

Detailed Design Document for the Martian Atmospheric General Circulation Model

F.Forget, F. Hourdin, R. Fournier, M. Collins, C. Hourdin, S. Lewis

November 9, 1999

Contents

1 Introduction **4**

2 Model Dynamics **4**
2.1 LMD grid-point dynamic model 4
2.2 AOPP grid-point dynamic model 5
2.3 Vertical discretization 5
2.4 Horizontal dissipation and sponge layers 5

3 Radiative transfer **7**
3.1 CO_2 gas 7
3.1.1 Thermal infrared. 7
3.1.2 Near infrared absorption. 7
3.2 Dust 8
3.2.1 Solar radiation. 8
3.2.2 Thermal infrared. 10
3.2.3 Visible/infrared opacity ratio. 15
3.2.4 Dust spatial distribution. 15
3.3 Net exchange formulation 16
3.3.1 General approach 16
3.3.2 Application to the Martian atmosphere 17
3.3.3 Example of net exchange computation 18

4 Surface and subsurface thermodynamics **20**
4.1 Subsurface conduction and heat storage 20
4.2 Surface properties 21

5 Turbulent diffusion in the planetary boundary layer **21**
5.1 Introduction 21
5.2 Temporal evolution of turbulent kinetic energy 22
5.3 Coupled stationary solution 23
5.4 Numerical scheme 25
5.5 Typical results 26

6 Convection **28**

7 Representation of Sub-Grid Scale Orography **28**
7.1 Introduction 28
7.2 Low Level Drag Parametrisation 29
7.3 Gravity Wave Drag 30
7.4 Sub-grid Scale Orographic Parameters 31

8 CO_2 condensation-sublimation Scheme **33**
8.1 Physics of the condensation-sublimation process 33
8.2 Numerical scheme 36

9 The "CO_2 snow scheme: Modeling the impact of the CO_2 clouds and fresh snow on the radiative budget **38**
9.1 Introduction: Clouds or snow? 38
9.2 Variation of the snow emissivity 40
9.3 Numerical scheme 42
9.4 Typical results 44

1 Introduction

This document is a scientific description of the LMD/AOPP General circulation model of the Martian atmosphere. It is based on the first "Detailed Design Document" written as part of Work Package II in early 1996. However, this document is aimed to provide a more complete view of the entire model, by gathering more mature descriptions recently published in several recent scientific papers (Collins et al. 1997, Forget 1998, Forget et al. 1998, 1999, Lewis et al. 1999).

The original LMD/AOPP Martian Atmospheric General Circulation Model had itself been described in previous publications (Hourdin, 1992b; Hourdin et al., 1993; Hourdin et al., 1995,) and the present document especially foccuss on the novel aspects which have been either developed or improved in the frame of the ESA contract. The General Circulation Models can be schematically devided into several parts, which are described in this document.

- A first part is an **hydrodynamical code** dedicated to the time and spatial integration of the equations of hydrodynamics to compute the large scale atmospheric motions.
- A second part of the code consists of a set of **physical parametrizations** which are used to force the general circulation and compute the details of the local climate at every grid point. This includes (1) **Radiative transfer**, which is the source of atmospheric motions ; (2) small scale motions not explicitly represented by the hydrodynamical code, such as the **turbulent diffusion in the planetary boundary layer**, **convection**, the **atmospheric drag due to the subgrid-scale orography**, and **gravity wave drag** ; (3) **surface and sub-surface thermodynamics** ; (4)**condensation and sublimation of atmospheric CO_2** and the corresponding **radiative effects of the CO_2 snow**.

2 Model Dynamics

The core of an atmospheric general circulation model is the hydrodynamical code dedicated to the time and spatial integration of the equations of hydrodynamics. This part, which is based on a rather general formulation of the hydrostatic primitive equations of dynamical meteorology on a sphere, can be adapted directly from terrestrial models. Two distinct formulations have been developed so far: 1.a finite-differences or grid point model, based on the discretization of the horizontal domain fields on a latitude-longitude grid ; 2. a spectral model, in which the horizontal model fields are represented by a truncated series of spherical harmonics.

Each of these formulations offers advantages and disadvantages with regard to accuracy and numerical performance, and both approaches are employed at various centres for climate modelling on Earth. As for Mars, since both formulations had been previously used at LMD (grid point model) and AOPP (spectral model), we chose to keep both kinds as options in order to estimate the likely uncertainty arising from certain types of modelling errors.

2.1 LMD grid-point dynamic model

The grid point dynamic model is based on the LMD terrestrial model described in Sadourny and Laval (1984). The discretization scheme conserves both potential enstropy for barotropic non-divergent flows (Sadourny, 1975) and total angular momentum for constant surface pressure axisymmetric flow. The latter property was not included in the original terrestrial version but was found to be very important

for simulating the Martian atmosphere in order to avoid spurious prograde zonal winds in equatorial regions (Hourdin, 1992b). The model is typically run with a regular resolution of 64×48 grid points horizontally, corresponding to 3.75^o latitude by 5.625^o longitude. However, in its present version, the grid points can be arbitrarily spread in both latitude and longitude. This offers the possibility of zooming in on a given part of the globe to study the local meteorology, for instance at a spacecraft landing site. At high latitude, a filter is applied near the singularity in the grid at the pole in order to satisfy the Courant-Friedrichs-Lewy numerical stability criterion without going to an excessively small time-step. In the original version of the dynamical code a classical Fourier filter was used but we found that, because the Martian polar atmosphere appears to be much more dynamically unstable than the Earth's polar atmosphere, a more efficient formulation (based on the grouping of adjacent grid-points together) was necessary to avoid numerical instability.

2.2 AOPP grid-point dynamic model

The AOPP spectral solver was originally developed at the University of Reading (Hoskins and Simmons, 1975), and also conserves total angular momentum. A triangular truncation in spectral space at total wavenumber 31, with the nonlinear terms calculated on a 96×48 real space grid, is typically used.

2.3 Vertical discretization

In the vertical, both models use the terrain-following σ-coordinate system (σ is pressure divided by surface pressure) in finite-difference form. The choice of the vertical grid is not straighforward since we want to have both a fine resolution near the surface allowing a better representation of the atmospheric boundary layer as well as a large vertical extension to reach an effective height of about 80-100 km. This extension not only allows us to explore the meteorological regime at these altitudes, but we found that a deeper model domain allows for the full development of the Hadley circulation and was thus necessary to properly simulate the Martian climate below 50 km (Forget et al. 1999).

This was acheived by using the following analytical function for the σ-levels

$$\sigma_l = \frac{1.}{1. + C\left[\exp E(l-1) - 1\right]} \tanh\left[\frac{.5 * (N+1-l)}{NH}\right] \qquad (1)$$

where N is the total number of layers.

The first term on the right hand side is close to a geometric progression near the surface (the ration between the thickness of two consecutive layers is about constant) and results in constant layer thickness (in meters) in the rest of the atmosphere. The tanh term is introduced in order to have a slow transition to a zero pressure over the NH upper layers of the model. E and C constants are computed from the thickness of the first layer and from the total atmospheric vertical extension. 25 levels are typically used. Table 1 gives the distribution of the 25 layers for a first layer 10 m thick, an effective vertical coverage of 80 km and 2 layers for the transition zone at the top, which was chosen for the database simulations.

2.4 Horizontal dissipation and sponge layers

In both the grid-point and spectral models, non linear interactions between explicitly resolved scales and subgrid-scale processes are parameterized by applying a scale-selective horizontal dissipation operator based on an n time iterated Laplacian Δ^n. For the grid-point model for instance, this can be written $\partial q/\partial t = ([-1]^n/\tau_{diss})(\delta x)^{2n}\Delta^n q)$ where δx is the smallest horizontal distance represented in

N	σ-levels		Altitudes (m)		
	Mid layer	Top	Mid Layer	Top	Thickness
1	0.9996	0.9990	3.6	10.0	10.0
2	0.9984	0.9972	16.4	28.1	18.1
3	0.9960	0.9939	39.8	60.9	32.8
4	0.9918	0.9880	82.1	120.5	59.6
5	0.9842	0.9774	159.0	228.1	107.6
6	0.9707	0.9587	297.9	421.3	193.2
7	0.9468	0.9264	547.0	764.1	342.8
8	0.9059	0.8728	988.4	1360.2	596.1
9	0.8392	0.7895	1753.3	2363.3	1003.0
10	0.7386	0.6725	3030.1	3967.7	1604.5
11	0.6042	0.5293	5037.8	6361.4	2393.6
12	0.4523	0.3812	7934.2	9644.6	3283.2
13	0.3101	0.2522	11708.6	13775.8	4131.3
14	0.1979	0.1557	16197.5	18598.4	4822.5
15	0.1201	0.9144×10^{-1}	21192.6	23921.1	5322.7
16	0.7050×10^{-1}	0.5189×10^{-1}	26522.0	29585.4	5664.3
17	0.4045×10^{-1}	0.2875×10^{-1}	32076.2	35491.2	5905.7
18	0.2282×10^{-1}	0.1561×10^{-1}	37802.0	41597.3	6106.1
19	0.1265×10^{-1}	0.8297×10^{-2}	43698.9	47918.4	6321.1
20	0.6870×10^{-2}	0.4284×10^{-2}	49805.5	54529.5	6611.1
21	0.3609×10^{-2}	0.2115×10^{-2}	56242.3	61588.5	7058.9
22	0.1808×10^{-2}	0.9687×10^{-3}	63156.2	69395.2	7806.7
23	0.8212×10^{-3}	0.3869×10^{-3}	71047.8	78572.4	9177.2
24	0.3282×10^{-3}	0.1125×10^{-3}	80217.5	90921.3	12348.9
25	0.6535×10^{-4}	0	96358.2	–	–

Table 1: Vertical resolution of the GCM chosen for the database simulations.

the model and τ_{diss} the dissipation time scale for a structure of scale δx. A similar operator is applied to the spectral model fields in spectral space. These operators are necessary to ensure the grid-point model numerical stability and to prevent a build-up of energy at the truncation limit of the spectral model. In practice, the operator is separately applied to 1) potential temperature, 2) the divergence of the flow, and 3) its vorticity. We respectively use $n = 2$, $n = 1$ and $n = 2$ in the grid-point model. In the nominal version of the spectral model, however, $n = 3$ is used for the three fields, following the guidelines in MacVean (1983).

In the upper levels, a sponge-layer is also used in both models in an attempt to reduce spurious reflections of vertically-propagating waves from the model top. Unlike the traditional Rayleigh friction formulation, this operates as a linear drag solely on the eddy components of the vorticity and divergence fields and is not scale-selective. The timescales on which it operates are typically half a day, one day and two days respectively at the three uppermost levels.

3 Radiative transfer

the Martian atmosphere can be affected by the presence of CO_2 gas, mineral dust, water vapor, water ice particles and CO_2 ice particles (the radiative effects of ozone should generally be negligible, Zurek et al. 1992). This section describes how the effects of gaseous carbon dioxide and suspended dust are included in the model at solar and infrared wavelengths. The radiative effects of water vapor are neglected, since the cold Martian atmosphere cannot sustain more than a few tens of precipitable micrometers of water. In reality, water vapor could slightly increase the gaseous infrared absorption of the lower atmosphere in the northern hemisphere in summer (Savijärvi, 1991). However, the associated error should be small compared to the uncertainties related to the dust radiative properties and spatial distribution. Similarly, the effect of water ice clouds are neglected. Water ice clouds can become optically thick on Mars, but their occurrence is thought to be quite limited in space and time. Nevertheless, new measurements may motivate the development of water cloud parameterizations in the future. The possible radiative effects of CO_2 ice particles during the polar night have been parameterized separately, as explained in Section 9.

3.1 CO_2 gas

3.1.1 Thermal infrared.

The treatment of absorption and emission by the strong CO_2 15-μm band is described in Hourdin (1992a). The radiative transfer equation is integrated using the wide-band model developed by Morcrette et al. (1986). In its current version, the scheme accounts for the Doppler broadening of the molecular lines at low pressure (significant above 50 km) but not for departures from local thermal equilibrium (LTE) (thought to be significant above 70-80 km, near the top of the model). Work is ongoing to include non-LTE effects on cooling in the model. The CO_2 15-μm band, extending from 11.5 to 20 μm, is divided into two wide bands representing a) the central strongly absorbing part (14.2-15.7 μm) and b) the wings.

3.1.2 Near infrared absorption.

Atmospheric heating due to absorption of solar radiation in the near-IR bands of CO_2 is negligible below 30 km but becomes considerable above 50 km. A simple parameterization has been included which is similar in its effect to heating rates

obtained in radiative transfer calculations performed by Lopez-Puertas and Lopez-Valverde (1995) which include non-LTE effects. At pressure $p_0 = 700$ Pa and for a mean Mars-Sun distance $r_0 = 1.52$ AU, the heating rate corresponding to a zero solar zenithal angle ($\mu = 0$) is taken to be:

$$\frac{\partial T}{\partial t}(p_0, r_0, 0) = 1.3 \text{ K / day} \tag{2}$$

The heating rate at other pressures p, Mars-Sun distance r and zenithal angle μ is then computed as follows :

$$\frac{\partial T}{\partial t}(p, r, \mu) = \frac{\partial T}{\partial t}(p_0, r_0, 0) \times \frac{r_0^2}{r^2} \sqrt{\frac{p_0}{p}\tilde{\mu}} \ (1 + \frac{p_{\rm NLTE}}{p})^{-1} \tag{3}$$

where $p_{\rm NLTE}$ is a pressure below which non-LTE effects are significant ($p_{\rm NLTE} = 0.0075$ Pa) , and $\tilde{\mu}$ the cosine of the solar zenith angle corrected for atmospheric refraction (we use $\tilde{\mu} = \sqrt{(1224\mu^2 + 1)/1225}$)). The effect of non-LTE is a strong decrease of the heating above 80 km. In theory, this simple parameterization is not completely consistent since the CO_2 heating is just added to other heating terms without reducing the solar flux available for dust and surface heating below. However, the corresponding maximum reduction of the solar incident flux is always lower than 1.5%, well below the level of other uncertainties related to the dust and the surface properties.

3.2 Dust

3.2.1 Solar radiation.

As in the original version (Hourdin et al. 1993, 1995), the radiative transfer equation accounting for the absorption and scattering of solar radiation by the dust is based on the numerical scheme of Fouquart and Bonel (1980). This code was originally developed for the LMD terrestrial GCM and is currently used by the operational model of the European Centre for Medium-Range Weather Forecasts (ECMWF). The upward and downward fluxes are obtained from the reflectances and transmittances of the layers, computed using the Delta-Eddington approximation.

Dust radiative properties at solar wavelengths The available studies of Martian dust optical properties have suggested that the single-scattering properties are characterized by an abrupt change around 0.5 μm near the peak of the incident solar flux, and that multispectral calculations were essential to obtain accurate results (Ockert-Bell et al., 1997). Since detailed multispectral calculations would be too expensive in a GCM, we use two broad bands (0.1-0.5 μm and 0.5-5 μm). Choosing the exact radiative properties to be used by the model remains problematic, however. On the one hand, this is due to the fact that the dust single scattering properties may vary with altitude, season and horizontal locations, and that the various properties obtained by the different past studies may not be representative. In particular, it is likely that in some conditions, the dust particles can get coated by water ice. On the other hand, the radiative transfer results which are of importance for the GCM (e.g. heating rates) are unfortunately extremely sensitive to the dust properties. For instance, the dust single scattering albedo ω at solar wavelength is thought to be quite high, typically around 0.9. An uncertainty of $\pm 5\%$ then corresponds to an error on the heating rate of about $\pm 50\%$...

The most complete dataset currently available is probably the spectral single-scattering properties extrapolated over the solar wavelengths by Ockert-Bell et al. (1997) from the Pollack et al. (1995) Viking Lander data (fig 1) These data appears to be consistent with the more recent Pathfinder observations (Markiewicz et al.,

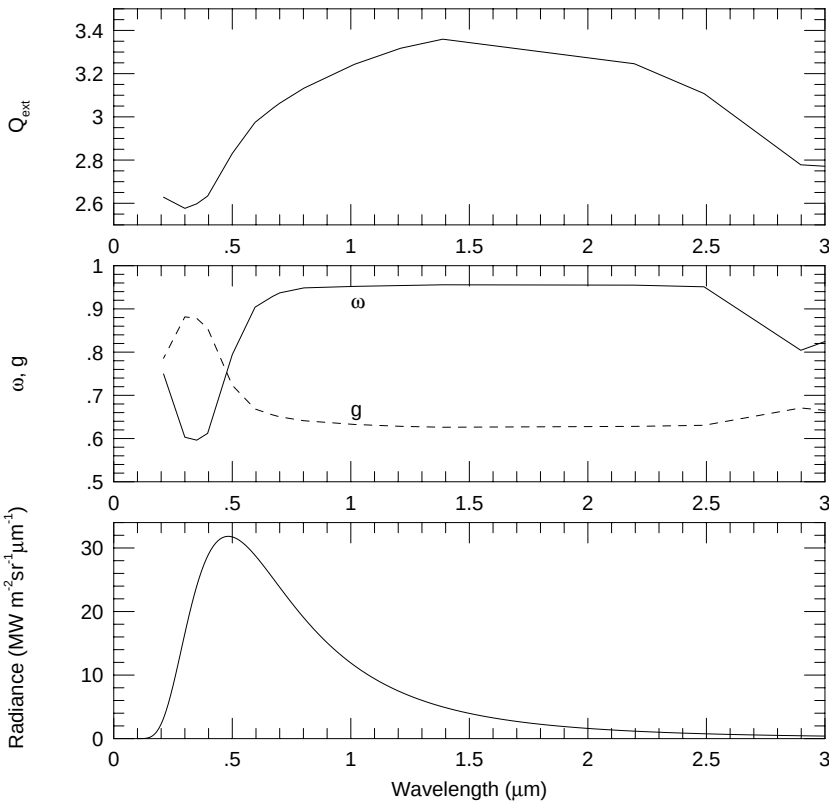

Figure 1: Martian dust single scattering properties at solar wavelength used to compute the wavelength integrated parameters in the GCM (from Ockert-Bell et al. ,1997). Q_{ext} is the extinction parameter, ω the single scattering albedo and g the asymmetry parameter. Also shown is the radiance of a blackbody at 6000 K, illustrating the incident solar radiation at the top of the atmosphere.

	Band	$\tilde{Q}_{\rm ext}/Q_{\rm ext}(0.67\mu{\rm m})$	$\tilde{\omega}$	$\tilde{g}$
Solar radiation (1)	0.1-0.5 μm	0.878	0.665	0.819
(Ockert-Bell et al. 1997)	0.5-5 μm	1.024	0.927	0.648
Solar radiation (2)	0.1-0.5 μm	1.0	0.920	0.55
(Clancy and Lee 1991)	0.5-5 μm	1.0	0.920	0.55
Thermal	5-11.6 μm	0.253	0.470	0.528
radiation	11.6-20 μm	0.405	0.541	0.551
(Forget 1998)	20-200 μm	0.166	0.370	0.362

Table 2: Averaged atmospheric dust single scattering parameters used in the solar and thermal infrared radiative transfer code in the current version of the model (computed from Ockert-Bell et al. 1997, Clancy and Lee 1991 and Forget 1998) with the infrared to visible opacity ratio $\tau_{9\mu m}/\tau_{0.67\mu m}$ set to 2. Given the uncertainties, two alternative sets of parameters have been used at solar wavelengths in the present work.

1999). In order to make use of such spectral data in the GCM wide band model, it is necessary to average them spectrally in each wide band to obtain mean scattering coefficients (extinction coefficient $\tilde{Q}_{\rm ext}$, single-scattering albedo $\tilde{\omega}$ and asymmetry parameter $\tilde{g}$). The following ponderation laws are used:

$$\tilde{Q}_{\rm ext} = \frac{\int_{\lambda_1}^{\lambda_2} B_\lambda Q_{ext,\lambda}\, d\lambda}{\int_{\lambda_1}^{\lambda_2} B_\lambda\, d\lambda} \quad (4)$$

$$\tilde{\omega} = \frac{\int_{\lambda_1}^{\lambda_2} B_\lambda Q_{{\rm ext},\lambda}\omega_\lambda\, d\lambda}{\int_{\lambda_1}^{\lambda_2} B_\lambda Q_{{\rm ext},\lambda}\, d\lambda} \quad (5)$$

$$\tilde{g} = \frac{\int_{\lambda_1}^{\lambda_2} B_\lambda Q_{{\rm ext},\lambda}\omega_\lambda g_\lambda\, d\lambda}{\int_{\lambda_1}^{\lambda_2} B_\lambda Q_{{\rm ext},\lambda}\omega_\lambda\, d\lambda} \quad (6)$$

where B_λ is the Planck function at 6000 K (representing the solar radiance) and λ_1, λ_2 the wavelengths at the boundaries of the band. The resulting parameters used in the model are shown in Table 2.

Alternative dust properties have been proposed by Clancy and Lee (1991) on the basis of their analysis of the Viking orbiter infrared thermal mapper (IRTM) emission-phase-function measurements. These observations, performed from above the atmosphere rather than from Landers in the case of the studies previously mentionned, yield brighter dust properties, with a higher single scattering albedo and a lower asymetry parameter (Table 2). Until better data from the upcoming Martian missions are made available, these properties have been used as an alternative set of parameters in the present model. They yield slightly colder temperatures than with the Ockert-Bell dust parameters. With the current version of the model, this appears to be more realistic when compared to the available observations.

3.2.2 Thermal infrared.

In the original version of the model, scattering of thermal infrared radiation was not taken into account because the radiation was assumed to be isotropic at all wavelength. This assumption is made in most Earth studies and is probably valid on Mars within the CO_2 15-μm band. However, we found that at other wavelengths, the infrared radiation scattered by the atmospheric dust back to the surface can be non-negligible (Fig. 2), thus changing the surface and atmospheric temperature.

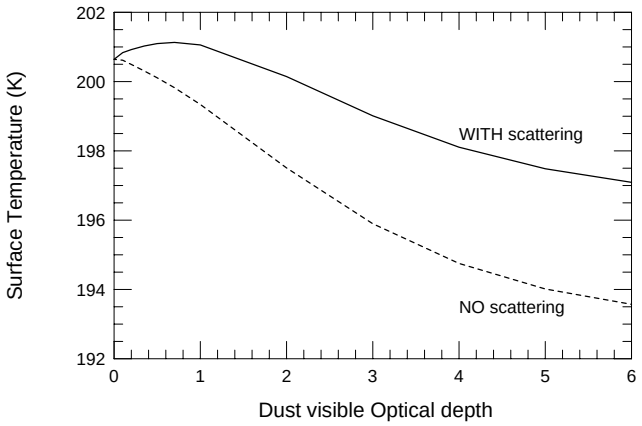

Figure 2: Daily averaged surface temperature computed at Viking Lander 1 site (22^oN) at winter solstice ($L_s = 270^o$) as a function of dust opacity (results obtained with a 1D radiative-convective version of the GCM physical package). Scattering of infrared radiation by the airborne dust typically increases the incident IR flux to the surface outside the CO_2 gaseous band by 10 to 20 %. this results in a warming of the surface.

We have therefore included a radiative transfer scheme that accounts for multiple scattering by dust particles outside the CO_2 15-μm band. It is based on the two-stream hemispheric mean source function code described by Toon et al. (1989). The infrared spectrum outside the CO_2 15-μm band is divided into two wide bands, one for the 9 μm silicate band (5-11.5 μm) and one for the rest of the infrared spectrum (20-200 μm).

Dust radiative properties at infrared wavelengths Until more accurate data are made available, we use a set of synthetic-single scattering spectral properties of the Martian dust specifically formulated for this GCM and described in Forget (1998). Several models of dust radiative properties at thermal wavelengths had been previously proposed in the literature (Toon et al., 1977, Clancy et al., 1995). However, most of them were designed to study the size or the composition of the dust particles rather than their impact on the radiative budget: the basic approach has been to assume that the optical indices were described by known Earth mineral or soil type. For instance, the long-standing Toon et al. (1977) model of Mars atmospheric dust is based on the use of the optical properties of a clay mineral sample called montmorillonite 219b. Unfortunately, none of these models can accurately reproduce the observation (e.g. the IRIS spectra obtained during the 1971 dust storm), especially around 20 μm where the blackbody emission is close to its maximum at Martian temperatures.

Therefore, our purpose being the best parametrization of the Martian dust from a radiative transfer point of view, we have designed a "synthetic" dust model without concern for the actual dust composition. Because the size distribution and the optical properties suggested by Toon et al. were able to closely match the observed 8 - 13-μm absorption band, we kept this model below 15 μm, and tried to improve it above 15 μm. What had to be improved ? The complex refractive indexes of the Toon et al. montmorillonite 219b are shown in fig. 3. The corresponding single scattering parameters, including the extinction coefficient $Q_{\rm ext}$, the single-scattering albedo ω and the asymmetry parameter g, deduced from the Mie theory are presented in fig. 4. The montmorillonite 219b is characterized by two absorption bands at 19 and 21 μm. Such bands are not apparent in the IRIS spectra of Mars atmo-

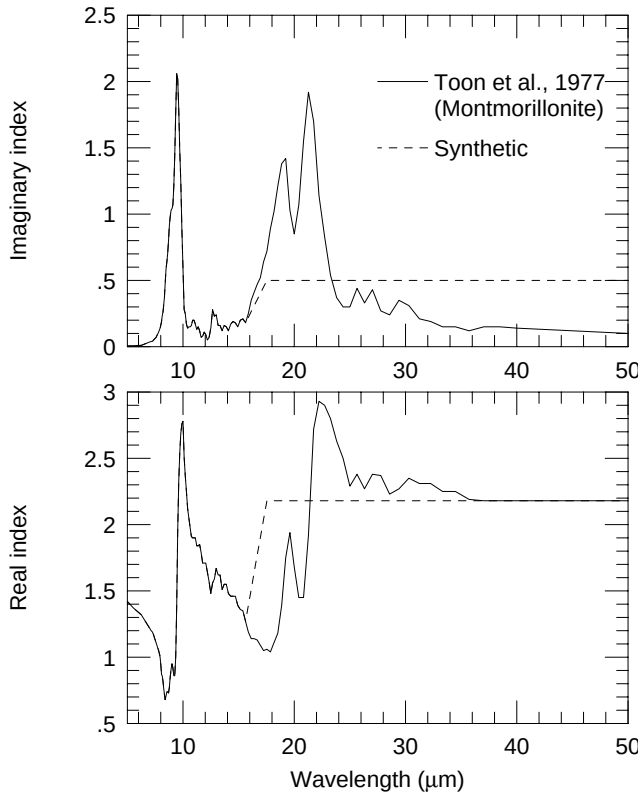

Figure 3: Refractives indexes of our "synthetic" model compared to the Toon et al. [1977] montmorillonite.

spheric dust. In fact, unlike the Si-O stretching fundamental band near 9-10 μm which appears in most silicates, these two bands are not universal. In particular, measurements by Roush et al. [1991] have shown that rock types thought to be close to the Martian rocks (palagonite, saponite) do not exhibit such bands. However, most of these minerals, including montmorillonite, are characterized by a real index of refraction near 2.2 beyond 30 μm.

Based on these considerations, we have tried to reproduce the IRIS observations just by fixing the real index at 2.18 (the montmorillonite real index in the far infrared) above 17 μm. The amount of atmospheric dust (characterized by the vertical dust optical depth) was estimated for each spectrum by fitting the observed 9 μm band. Following this protocol, we have found that very good results could be obtained for the four spectra with a constant imaginary index of 0.5 over the same spectral region (figs. 3). The corresponding Mie single scattering properties are shown along with the Toon et al. data in figure 4. In reality, it is unlikely that the imaginary index remain exactly constant up to very high wavelengths. According to the Kramer-Kronig dispersion relation, the imaginary index should slightly decrease with wavelength in the very far infrared if the real index is constant. However, since our goal is to determine the single scattering properties rather than the actual index of refraction a modelled, ideally constant index appear to be satisfactory for our purpose.

The ability of the new dust model to reproduce the observations is shown in figure 5. At any wavelength, the difference between the modeled and observed brightness temperatures is lower than 2 K. The four spectra were fitted using a dust optical depth at 9 μm near 1 (0.92, 1.30, 1.12, 1.05 respectively). Thus, the

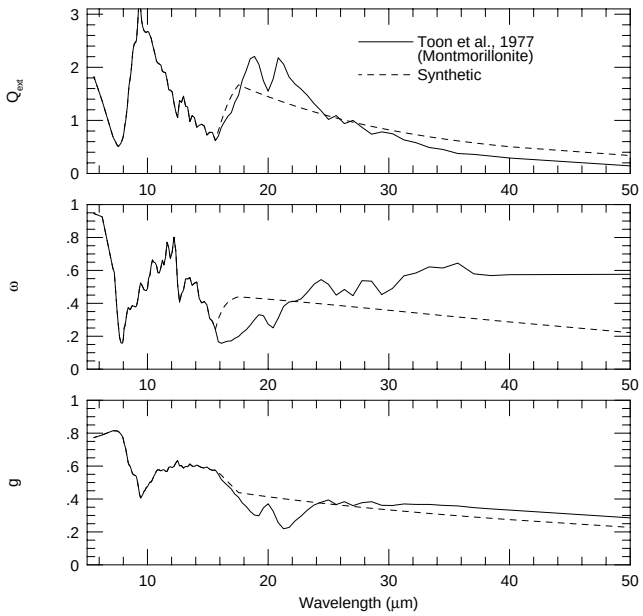

Figure 4: Single scattering properties of our synthetic dust model compared to the Toon et al. [1977] model. Q_{ext} is the extinction parameter, ω the single scattering albedo and g the asymmetry parameter.

impact of the scattering by the dust, which mostly depends upon the dust optical depth, is of the same order in the four cases: a brightness temperature decrease by about 5 to 8 K between 20 and 40 μm (based on calculations performed with an isothermal temperature profile). On the opposite, the decrease of radiance due to absorption and emission by dust particles colder than the surface is not the same in the four cases. This is due to the fact that the temperature gradient strongly varies with location and time. For instance, the temperature difference between the surface and the "top" of the emitting atmosphere is about 25 K for spectra 1 and 2, and almost 50 K for spectrum 3, spectrum 4 being in between. The fact that our dust model is able to accurately fit the four spectra in spite of these differences is worth emphasizing. In two cases (spectra 1 and 2), the dust signature is dominated by scattering, with a strong constraint on real index, and in an other case (spectrum 3), by absorption, with a strong constraint on the imaginary index. A counter-example is provided by the Toon et al. montmorillonite model beyond 30 μm. The agreement is good in the scattering cases (spectra 1 and 2), whereas the model strongly overestimate the brightness temperatures in the absorbing case (spectrum 3), indicating that the imaginary index of montmorillonite is too low in this spectral region.

In each wide band, wavelength-integrated mean dust single-scattering properties were computed using Eq. 4, 5 and 6, with B_λ the blackbody intensity at 215 K, a typical mean temperature on Mars (Table 2). This discretization in two wide bands was found to introduce less than 10% error compared to a more sophisticated narrow band computation. In the 15-μm band, absorption by the dust is added to the absorption by CO_2, using a mean absorption parameter $\tilde{Q}_{\rm abs} = (1-\tilde{\omega})\tilde{Q}_{\rm ext}$ with $\tilde{\omega}$ and $\tilde{Q}_{\rm ext}$ computed as above.

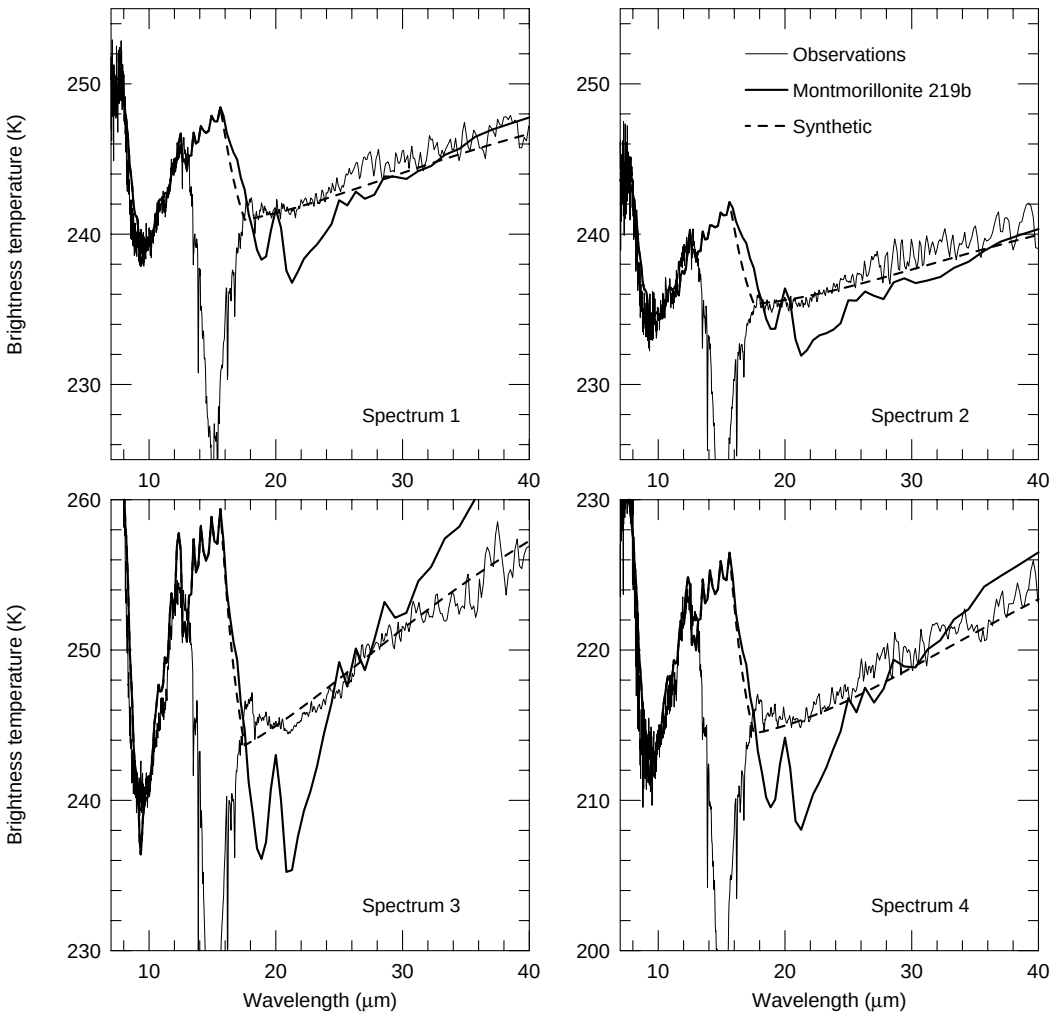

Figure 5: Comparison between four "dusty" IRIS spectra and modeled spectra computed with the Toon et al. [1977] model and our new synthetic model.

3.2.3 Visible/infrared opacity ratio.

The scaling of dust opacity in the infrared compared to the visible is also a key parameter of the dust model, since it controls the local radiative balance of the atmosphere and the surface. This ratio is highly sensitive to the actual dust size distribution, which is poorly known since each spectral region is sensitive to different particle sizes (see Zurek 1982, Forget 1998). In the original model, a ratio of about 1.2 had been used, following Pollack et al. (1979) as in most other existing Mars GCMs then (e.g. Pollack et al. 1990, Wilson and Hamilton 1996). However, measurements of the dust optical depth made separately at solar and infrared wavelengths at the same time and location suggest a visible (0.67μm) to infrared (9μm) ratio of about 2 to 2.5 (Martin 1986, Clancy et al. 1995). In the baseline version of the model, we therefore scale the dust opacities τ from the ratio $\tau_{9\mu m}/\tau_{0.67\mu m} = 2$ (Table 2).

3.2.4 Dust spatial distribution.

In the baseline version of the model, the dust mixing ratio is prescribed and the dust is not transported by winds (other versions of the model now include this capability, Forget et al. 1998a). The dust mixing ratio is taken to be constant in the lower atmosphere up to a level above which where it rapidly declines, consistently with the available spacecraft observations. Following Pollack et al. (1990), most GCMs (including the previous version of this model) have used the dust vertical distribution derived by Conrath (1975) from considerations of particle sedimentation and eddy mixing. The dust mass mixing ratio q was defined as a function of pressure p - that is,

$$\begin{aligned} q &= q_0 \exp[\nu(1 - p_0/p)] \quad (p \leq p_0) \\ q &= q_0 \quad (p > p_0) \end{aligned} \tag{7}$$

where q_0 is a constant determined by the prescribed optical depth at the reference pressure level $p_0 = 700$ Pa, and ν is a constant that determines the shape of the function. Conrath (1975) estimated $\nu = 0.007$ during dust storms, but Pollack et al. (1990) (and following most other GCMs) used $\nu = 0.03$ thought to represent more typical conditions. In reality, observations at the limb by the camera aboard Mariner 9 (Anderson and Leovy 1978) and Viking (Jaquin et al. 1986) have shown that the dust vertical distribution strongly varies with space and time, with dust confined near the surface in the polar regions or reaching very high altitudes in the tropics during dust storms. Representing these variations with Eq. 7 by varying ν would have led to an unrealistic vertical distribution. We therefore used a modified version of Eq. 7:

$$q = q_0 \exp[0.007(1 - p_0/p)^{(70/z_{max})}] \quad (p \leq p_0) \tag{8}$$

where z_{max} is the altitude (km) of the top of the dust layer. Equation 8 matches Equation 7 under the conditions for which the later was originally designed by Conrath ($\nu = 0.007$, $z_{max} = 70$ km) but remains realistic for thinner dust layers. The climatological altitude of the top of the dust layers can be deduced from the analysis by Anderson and Leovy (1978) and Jaquin et al. (1986). To first order, these measurements can be summarized and represented by the function $z_{max} = 60 + 18\sin(L_s - 160^o) - 22(\sin\phi)^2$, with L_s the solar longitude and ϕ latitude. This equation is currently used in most of our simulations. However, we usually keep the reference mixing ratio q_0 constant horizontally over the planet. Indeed, although slight spatial variations of the dust optical depth have been measured by Martin

(1986) and Martin and Richardson (1993), no simple dependence on latitude or longitude can be determined.

3.3 Net exchange formulation

Recently, at LMD, in the frame of extension to ESA Contract 11369/95/NL/JG, the infrared part of the radiative transfer code has been rewritten with a net exchange formulation.

3.3.1 General approach

The net exchange formulation is firstly an integral formulation in which the radiative budgets are addressed directly without explicit formulation of the radiative intensity field. If the full system is discretized in N surface or volume elements E_i, the radiative budget of element i can be formally written as

$$\psi_i = \sum_{i \neq j} \phi_{j,i} - \mathcal{E}_i \tag{9}$$

where $\mathcal{E}_i$ is the total radiative power emitted by i and $\phi_{j,i}$ is the radiative power emitted by j and absorbed by i (exchange). In the net exchange formulation, the emitted power $\mathcal{E}_i$ is no longer considered as a whole but also split into the $N-1$ exchanges toward the other elements as

$$\mathcal{E}_i = \sum_{i \neq j} \phi_{i,j} \ . \tag{10}$$

The radiative budget of element i then writes

$$\psi_i = \sum_{i \neq j} \psi_{i,j} \tag{11}$$

where $\psi_{i,j} = \phi_{j,i} - \phi_{i,j}$ is the individual net exchange of radiative power between i and j.

As flux formulations, net exchange formulations are intrinsically energy conserving. In the first case, conservation is obtained from the final differentiation of radiative fluxes. In the net exchange formulation conservation ($\sum_i \psi_i = 0$) is more constraining relying on the reciprocity of individual exchanges ($\psi_{i,j} = -\psi_{j,i}$). A direct consequence is that different approximations can be used for the various exchanges without violating neither conservation nor reciprocity. More generally, the net exchange formulation is a powerful analysis frame allowing in particular to quantify the relative importance of the various terms. Note finally that, in quasi isothermal conditions, flux formulations ends with the differentiations of a quasi-constant flux whereas net exchange formulations compute the sum of small residuals avoiding some numerical problems.

In the general case, $\psi_{i,j}$ is the sum of partial net exchanges at all frequencies and along all possible optical paths between E_i and E_j. Corresponding formulations include complex spectral and optico-geometric integrals that may resumed as (Dufresne et al., 1998,)

$$\psi_{i,j} = \int_0^{+\infty} d\nu \int_{\Gamma_{i,j}} d\gamma \tau_\gamma^\nu K_{1,\gamma}^\nu K_{2,\gamma}^\nu \left(B_{1,\gamma}^\nu - B_{2,\gamma}^\nu \right) \tag{12}$$

In this expression, $\Gamma_{i,j}$ is the space of all optical paths with first and second extremities within E_i and E_j respectively. For each optical path, τ_γ^ν is the total

transmittance function along the path, $B^{\nu}_{1,\gamma}$ is the spectral black body intensity function at the first extremity and $K^{\nu}_{1,\gamma}$ is either the absorption coefficient (if E_i is a volume element) or the directional emissivity (if E_i is a surface element) at the first extremity. The index 2 is used similarly for the second extremity. As will be illustrated later, net exchange rates are valuably interpreted along this line: local temperature differences and emission properties define exchange potentials that must be associated with optico-geometric constraints (possible optical paths, extinction) to analyze the physics of infrared radiation exchanges between considered elements.

Net exchange formulations automatically insure two important (and equivalent?) properties of radiative transfer : reciprocity ($\psi_{j,i} = -\psi_{i,j}$) and energy conservation ($\sum_i \sum_j \psi_{i,j} = 0$).

3.3.2 Application to the Martian atmosphere

For Marian GCM studies restricted to the $15\mu m$ CO_2band, assumptions can be retained that allow very significant simplifications of the geometric: the atmosphere can be assumed perfectly stratified along the horizontal, "effect mirage" as well as molecular and particulate scattering can be neglected, the boundaries (space and planetary surface) are assimilated to black body surfaces (with a temperature of 0 K for space). Under these assumptions, the space of relevant optical paths reduces to straight lines between exchange positions. Dividing the atmosphere into N layers, net exchange rates can be derived as

- exchange between two layers

$$\psi^{\nu}_{i,j} = \int_{z_{i-\frac{1}{2}}}^{z_{i+\frac{1}{2}}} \int_{z_{j-\frac{1}{2}}}^{z_{j+\frac{1}{2}}} (B^{\nu}_{z_j} - B^{\nu}_{z_i}) \left| \frac{\partial^2 \tau_{\nu}(z_i, z_j)}{\partial z_i \partial z_j} \right| dz_i dz_j \tag{13}$$

- exchange between a layer and boundaries

$$\psi^{\nu}_{i,b} = \int_{z_{i-\frac{1}{2}}}^{z_{i+\frac{1}{2}}} (B(T_b) - B^{\nu}_{z_i}) \left| \frac{\partial \tau_{\nu}(z_i, z_b)}{\partial z_i} y \right| dz_i \tag{14}$$

  with $T_b = T_{surf}$ for exchange with the planetary surface and $T_b = 0$ K for the cooling to space.

where $z_{i-\frac{1}{2}}$ and $z_{i+\frac{1}{2}}$ are the altitudes at the boundaries of atmospheric layer i and the monochromatic integrated transmission function τ_{ν} is defined as

$$\tau_{\nu}(z, z') = 2 \int_0^{\frac{\pi}{2}} \exp\left(- \int_z^{z'} k_{\nu}(z) \rho(z) \frac{1}{\cos\theta} dz \right) \sin\theta \ \cos\theta \ d\theta \tag{15}$$

where ρ is the air density and k_{ν} is the monochromatic absorption coefficient.

Computation of such integrals requires three types of numerical integrations.

- The angular integration is computed by applying the diffusive approximation which consists in the use of a mean angle (**?**, $1/\cos\theta = 1.66$, see)]Elsa:42.
- The frequency integration is approximated by a wide band model of transmission (Hourdin, 1992b,). In what follows, the model will be used as a narrow rather than wide band model which means that the planck function is constant enough on the interval so that it can be taken off the integral. This point is discussed further later on.
- The vertical integration is what we concentrate on in the rest of the text with various levels of approximation.

This simplification was shown to produce minor errors in martian computations.

	σ	Approximate Height		σ	Approximate Height
1	0.999907	3.6 m	14	0.659718	16.1976 km
2	0.999579	16.4 m	15	0.580298	21.1927 km
3	0.998980	39.8 m	16	0.506077	26.5220 km
4	0.997893	82.1 m	17	0.438807	32.0763 km
5	0.995924	159.0 m	18	0.378806	37.8021 km
6	0.992380	297.9 m	19	0.325576	43.6990 km
7	0.986050	547.0 m	20	0.278323	49.8056 km
8	0.974939	988.4 m	21	0.235920	56.2423 km
9	0.955975	1.7533 km	22	0.197541	63.1562 km
10	0.925138	3.0301 km	23	0.161305	71.0479 km
11	0.878650	5.0378 km	24	0.127463	80.2175 km
12	0.815669	7.9343 km	25	0.084210	96.3582 km
13	0.740321	11.7087 km			

Table 3: σ levels and approximate heights based on -10ln(σ)

3.3.3 Example of net exchange computation

We present a numerical computation of net exchanges for 25 atmospheric layers (typical vertical discretisation of GCMs) with an enhanced resolution near the surface (see table 3) and for a typical temperature profile derived from Viking entry profiles (Seiff, 1982,) and refered to as perturbed profile by (Hourdin, 1992b). The atmosphere is assumed to be dust-free and the surface pressure is fixed to 700 Pa. For this computation, the vertical integrals are computed by dividing each of the 25 layers into 20 sub-layers, taking into account subgrid-scale temperature variations (see Fig. 6).

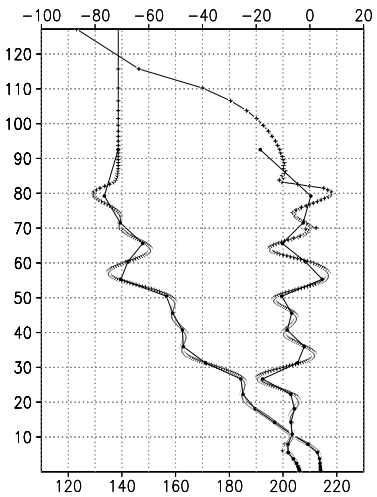

Figure 6: Typical temperature profile. 500 sublayers and 25 layers.

Fig. 7 displays a graphical representation of the radiative exchange in the atmosphere. More precisely, each element of the matrix displays the intensity of the net exchange rate between each pair i, j. This net exchange $\chi_{i,j}$ is expressed in Kelvin per Day:

$$\chi_{i,j} = \frac{g}{Cp} \frac{1}{\delta t} \frac{\psi_{i,j}}{\delta p_i} \tag{16}$$

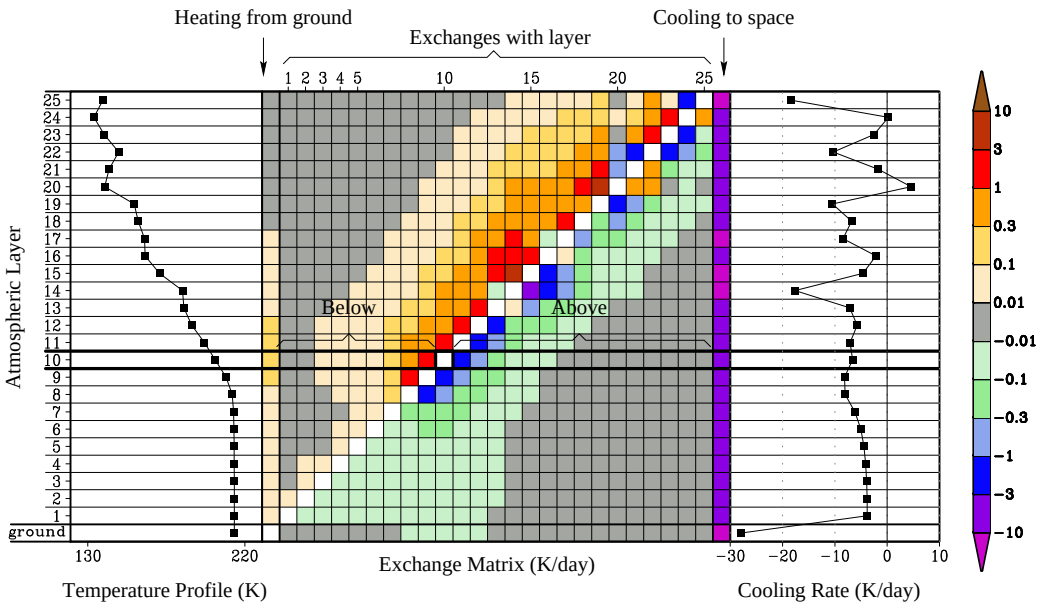

Figure 7: Graphical representation of the radiative exchanges in the Martian atmosphere.

(where g is the gravity, Cp the massic heat capacity, and δt the length of the day. The cooling rate of a layer i is:

$$\chi_i = \sum_j \chi_{i,j} \tag{17}$$

As an example for reading Fig. 7, consider layer $i = 10$ (highlighted in the figure). The left curve gives its temperature, the matrix line gives the exchange values $\chi_{i,j}$ between layer i and layers j (including ground and space), and the right curve gives its cooling rate χ_i which is just the sum of all exchanges values $\chi_{i,j}$ on line i (cf Eq. 17). Layer 10 is heated by the warmer underlying atmosphere and surface and looses energy toward the colder layers above and toward space. Note that the picture is more complex in the upper atmosphere where the wavy structure of temperature tends to be dumped by exchanges between nearby layers (a warmer layers cools toward nearby colder layers).

More generally $\chi_{i,j}$ and $\chi_{j,i}$ are of opposite sign. It means that when layer i loses energy to layer j, this layer j gains energy from layer i. In fact, the net exchange matrix expressed in $W.m^{-2}$ is exactly anti-symmetrical ($\psi_{i,j} = -\psi_{j,i}$).

More importantly, the net-exchange approach allows to quantify the relative importance of the various terms. The most important loss is the exchange with space: we thus obtain the classical result that the radiative heat budget of a layer is dominated by the cooling-to-space. Further, we see that the net exchange generally decreases with increasing distances. If the two layers under consideration are assumed to be isothermal (allowing to take the Planck functions off the integrals) the net exchange is the product of two terms : 1) difference in Planck functions which generally increases with distance between layers (as temperature difference), and 2), an optical factor $\left|\frac{\partial^2 \tau_\nu(z_i,z_j)}{\partial z_i \partial z_j}\right|$ which is a monotone decreasing function of distance. The figure shows that the net exchange decreases with distance, which means that this decreasing function is the dominating term.

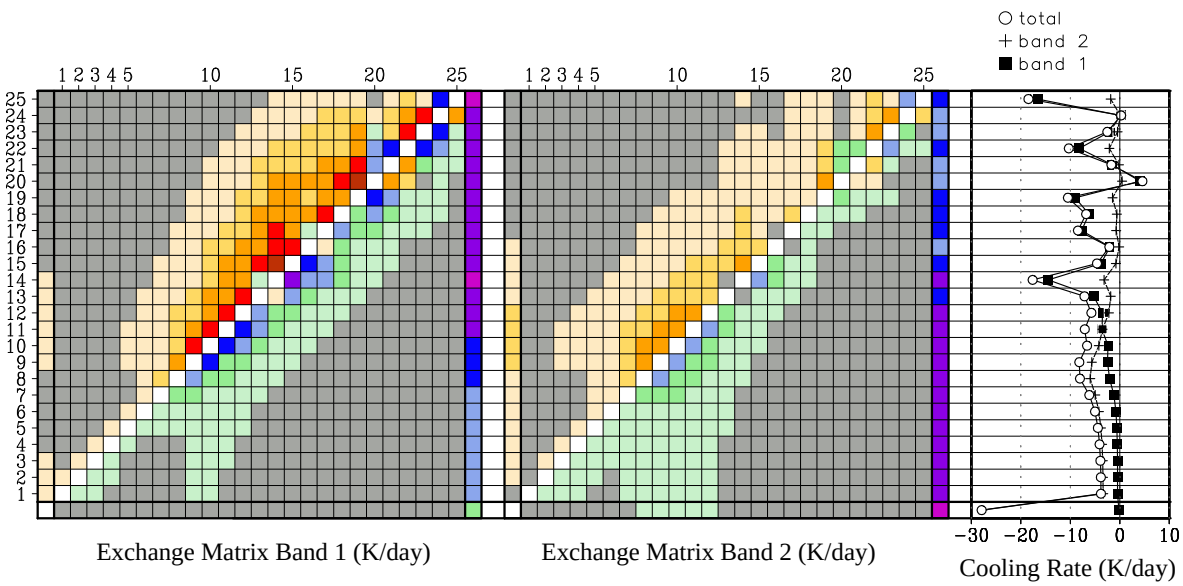

Figure 8: Exchange matrix for each CO_2band and corresponding vertical cooling profiles: total, band 1 and band 2

The main interest of this new method is first to allow analysis of the relative importance of the various terms included in the budget (in the flux formulation, we just have a global value for the exchange of the considered layer with all the rest of the atmosphere), and second to save CPU time. Indeed, we can compute less often the optical coefficients since they vary slowly in time. The Planck function, which varies more quickly, can easily be computed more often, because it is just a polynomial approximation. This new method is less costly and more accurate.

4 Surface and subsurface thermodynamics

4.1 Subsurface conduction and heat storage

Surface temperature evolution is governed by the balance between incoming fluxes (direct solar insolation, thermal radiation from the atmosphere and the surface itself, and turbulent fluxes) and thermal conduction in the soil. The parameterization of this last process is based on the sophisticated 11-layer soil model originally developed for the LMD Martian GCM (Hourdin et al., 1993).

The time evolution of the temperature under the surface is given by a classical conduction equation

$$\frac{\partial T}{\partial t} = -\frac{1}{C}\frac{\partial F_c}{\partial z} \tag{18}$$

where the conductive flux F_c is given by

$$F_c = -\lambda \frac{\partial T}{\partial z} \tag{19}$$

and where λ and C are the soil conductivity and specific heat per unit volume, respectively. In the simple case of a vertically homogeneous soil (which is assumed here), it can easily be shown that the model, as far as the time evolution of the surface temperature is concerned, is only dependent on the soil thermal inertia $I = \sqrt{\lambda C}$.

Although atmospheric GCMs often use force-restore schemes with one or two layers to simulate the time evolution of the surface temperature, it is much more accurate and straightforward to perform a direct temporal integration of these equations using a multi-layer difference scheme in the ground (Jacobsen and Heise, 1982; Warrilow et al., 1986). This was found to be numerically cheap enough even for a large number of layers in the soil: with 11 levels, this parametrization only represents 0.1% of the CPU-time of the Martian GCM. The soil model is similar to that presented by Warrilow et al. (1981). The accuracy of the model was checked by computing the phase and intensity of the surface temperature oscillation forced by a sin varying surface flux. For periods in the range from 0.3 to 2000 sols, the model produces errors of les s than 1% on the intensity and phase shifts lower than $.02\pi$.

4.2 Surface properties

A vertically homogeneous soil is assumed, and the spatially varying soil and surface properties, i.e. thermal inertia and albedo, are currently based on the Viking IRTM observations analyzed by Palluconi and Kieffer (1981) (thermal inertia) and Pleskot and Miner (1982) (albedo) extended to the polar regions using the recent results from Paige et al. (1994) and Paige and Keegan (1994). It has been suggested that the thermal inertia deduced by Palluconi and Kieffer (1981) may be overestimated due to weaknesses in the retrieval model (Haberle and Jakosky 1991) but it is retained for the present in the absence of more reliable information. More accurate data from the upcoming missions will be adopted as soon as available. A third map is used by the model for the surface orography. Unfortunately, the Martian orography is also poorly known. The accurate measurements expected from the Laser Altimeter (MOLA) aboard Mars Global Surveyor will be a great improvement for Martian climate models when available. Until then, two different data sets can be used by modellers: the Mars Consortium (Wu 1978) and the USGS digital elevation model (often called DTM ; see Davies 1992). The eigth-degree and order spherical harmonic model recently derived from radio occultation data by Smith and Zuber (1996) does not seem appropriate because of its low resolution. The choice between DTM and Consortium is controversial. Until recently, most GCMs, and in particular the LMD GCM, had used the Consortium dataset. However, this dataset suffers from the absence of coverage of the south polar region which is of key importance for the CO_2 cycle (Forget et al. 1998b). Thus, we now use the more recent DTM dataset which accounts for very fine structures not represented in the Consortium. Its main weaknesses are substantial biases on large scales. For instance, the DTM at its full resolution predicts that the Viking Lander 2 is about 1 km higher than that of Viking 1, whereas the mean pressure difference between the two sites indicate that Viking 2 is actually about 900 m below Viking 1.

5 Turbulent diffusion in the planetary boundary layer

5.1 Introduction

Accurate description of near surface conditions is a requirement for Martian GCMs in order to predict accurate surface drags, dust lifting, tracer transport and near-surface conditions for mission design. However, Mars is a challenging planet for parametrisation of boundary layer dynamics, the very shallow (about 100 m) and strongly stratified nocturnal boundary layer evolving during the day in a very deep and fully convective layer of several kilometers.

As in most GCMs, boundary layer dynamics is accounted for by a turbulent closure scheme based on the concept of turbulent viscosity plus a convective adjustement in case of unstable temperature profiles (see below). The turbulent mixing of any state variable a (horizontal wind components or potential temperature) is computed as

$$\frac{\partial a}{\partial t} = \frac{1}{\rho}\frac{\partial}{\partial z}K\rho\frac{\partial a}{\partial z} \tag{20}$$

where K takes different values K_u and K_θ for (u, v) and θ respectively. At the surface, the turbulent surface flux of heat and momentum is computed as the product between the vertical gradient of the quantity (estimated between the surface value and that in the first atmospheric layer) and a simple drag coefficient C_d given by:

$$C_d = \left(\frac{k}{\ln\frac{z}{z_0}}\right)^2 \tag{21}$$

where z_0 is the roughness length (1 cm in the baseline version of the GCM), z is the height of the middle of the first atmospheric layer and $k = 0.4$ is the von Karman constant. (C_d does not depend on the near surface temperature profile because of the small depth of the first layer in the model ($z_1 \sim 4$ m): It has been assumed that the wind profile in the first meters above the surface is logarithmic).

The scheme has been recently improved by introducing a new parametrisation for K_u and K_θ. This improvement is described here in details, with the following section:

i) description of the turbulent kinetic energy evolution equation (Sec. 5.2) ;

ii) description of the assumptions underlying the parametrisation scheme (Sec. 5.3) ;

iii) description of the algorithm (Sec. 5.4).

5.2 Temporal evolution of turbulent kinetic energy

Mellor and Yamada (1982) (see also Helfand and Labraga, 1988) have proposed a set of models of turbulent kinetic energy evolution in planetary boundary layers. The most commonly used as good compromise between accuracy and computational requirements is named the Mellor and Yamada 2.5 model : this model is a second order closure model that accounts for turbulent thermoconvection in stratified stable or unstable conditions.

The following notations are used. q is a representation of the wind standard deviation associated to turbulent fluctuations. $E = \frac{q^2}{2}$ is the turbulent kinetic energy. l is a length scale representative of large scale structures ; it is called the master length scale. M is the mean shear :

$$M = \sqrt{\left(\frac{\partial u}{\partial z}\right)^2 + \left(\frac{\partial v}{\partial z}\right)^2} \tag{22}$$

G_M and G_H are the dimensionless square of the mean shear and the negative of the dimensionless square of the Brunt-Vaisala frequency :

$$G_M = \frac{l^2}{q^2}M^2 \tag{23}$$

and

$$G_H = -\frac{l^2}{q^2}\frac{g}{\theta_0}\frac{\partial\theta}{\partial z} \tag{24}$$

where u and v are the components of horizontal velocity, θ is the potential temperature and θ_0^{-1} is the coefficient of thermal expansion. Two stability functions S_M

and S_H are also introduced in the original Mellor and Yamada 2.5 scheme that are direct functions of G_M and G_H. However Galperin et al. (1988) have proposed new expressions that are functions of G_H only :

$$S_M = \frac{0.393 - 3.09 G_H}{1 - 40.8 G_H + 212 G_H^2} \tag{25}$$

and

$$S_H = \frac{0.494}{1 - 34.7 G_H} \tag{26}$$

These stability functions have been tuned experimentally so that turbulent diffusion coefficients for velocity and potential temperature are respectively :

$$K_M = q l S_M \tag{27}$$

and

$$K_H = q l S_H \tag{28}$$

When assuming that the vertical diffusion of turbulent kinetic energy is negligible compared to local sources and sinks, the temporal evolution of turbulent kinetic energy may be written :

$$\frac{l}{q^3}\frac{\partial E}{\partial t} = S_M G_M + S_H G_H - \frac{1}{B_1} \tag{29}$$

where B_1 is a constant of proportionality taken as $B_1 = 15.0$. This set of equations is closed when specifying the master length scale. We retained Blackadar's formula (Blackadar, 1962) with $l_0 = 160m$:

$$l = \frac{\kappa z}{1 + \frac{\kappa z}{l_0}} \tag{30}$$

where κ is von Karmans constant.

Figures 9a and c show results from one-dimensional simulation obtained with this model with the same vertical discretisation as for a 3D GCM simulations. The vertical wind and temperature structures are similar to those obtained by Haberle et al. (1993a) with a strong decrease of the planetary boundary layer height at night and an associated nocturnal jet with wind magnitudes 20 % above the large scale geostrophic wind.

5.3 Coupled stationary solution

In the reference parametrisation presented above, we use an implicit time scheme except for K. However, even with this classical implementation, the model requires very small time steps (here about 1000 times longer than in the GCM), especially at night. The instability in those strongly stratified conditions was attributed to the strong coupling between wind shear and TKE : for large time steps, the TKE evolution cannot be estimated witout taking into account the wind shear reaction during the time step.

A first solution could be the use of Mellor and Yamada 2.0 model in which it is assumed that the turbulent kinetic energy takes its stationary solution (Helfand and Labraga, 1988). Tests in strongly stratified configurations indicated that this assumption is not realistic. Despite the fact that time constantes of Eq. 29 are very small, the stationary solution is meaningless because of the strong coupling with the wind profile. The assumption that time constants of turbulence establishment are very small compared to GCM time steps is valid but this establishment is a process that is strongly coupled to local wind shear evolution. This means that M

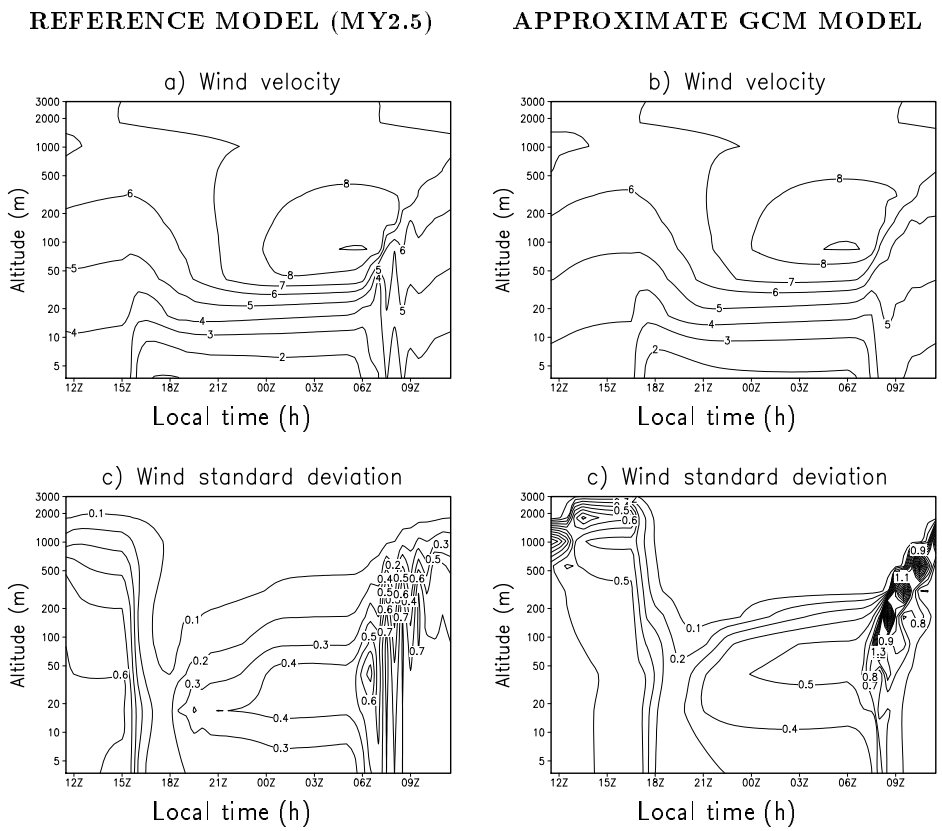

Figure 9: (a)(b)Horizontal wind mean velocity (m s^{-1}) and (c)(d) standard deviation of wind strength q due to turbulence (m s^{-1}) simulated by the reference Mellor and Yamada 2.5 model (left) and the proposed parameterization (right) useable with the GCM's 30 minute timestep. Results in both cases were obtained with a 1D version of the GCM physical package for conditions at the Viking Lander 1 site (22^{o}N) in spring ($L_s = 45^o$). The model is forced thermally by radiation (visiblen dust opacity: 0.5 ; surface albedo: 0.32 ; surface thermal inertia: 290 J m^{-2} $s^{-1/2}$ K^{-1}) and dynamically by a geostrophic wind of 7 m s^{-1}.

(that appears through G_M in the right side of Eq. 29) is a function of q that cannot be assumed constant when looking at stationary solutions of the turbulent kinetic energy.

On the one hand, M is not a direct function of q and the stationary solution of Eq. 29 coupled with wind shear evolution cannot be found simply. On the other hand, time constants of Eq. 29 are so small that its unstationary resolution requires small time steps incompatible with GCM requirements.

The proposed scheme assumes a simplified evolution law for M as a function of time and q : $M = M(q,t)$. This allows the stationary resolution of Eq. 29 in a way that accounts for responses of local wind shear to turbulent kinetic energy variations. For this purpose, we assume that the coordinate system is oriented in such a way that $v = 0$ (which allows to write $M = \frac{\partial u}{\partial z}$) and we write that the horizontal wind tendency due to turbulent diffusion is :

$$\left(\frac{\partial u}{\partial t}\right)_{diff} = \frac{\partial}{\partial z}\left(K_M \frac{\partial u}{\partial z}\right) = \frac{\partial}{\partial z}\left(K_M M\right) \tag{31}$$

Consequently, the wind shear tendency due to turbulent diffusion is :

$$\left(\frac{\partial M}{\partial t}\right)_{diff} = \frac{\partial^2}{\partial z^2}\left(K_M M\right) \tag{32}$$

and we observed that q could be estimated as the coupled stationary solution of Eq. 29 and Eq. 32 :

$$S_M G_M + S_H G_H - \frac{1}{B_1} = 0 \tag{33}$$

and

$$\frac{\partial^2}{\partial z^2}\left(K_M M\right) = 0 \tag{34}$$

5.4 Numerical scheme

The system of equations (Eq. 33,Eq. 34) has two unknowns q and M. All other quantities are assumed constant. Eq. 34 is discretised and when computing q_i and M_i at the i-th atmospheric layer interface, the assumption is made that q_{i-1}, M_{i-1}, q_{i+1} and M_{i+1} are constants. Eq. 34 can therefore be written as

$$K_{M,i} M_i = F \tag{35}$$

where F is a constant wind flux :

$$F = \frac{\frac{1}{dz_i} K_{M,i+1} M_{i+1} + \frac{1}{dz_{i-1}} K_{M,i-1} M_{i-1}}{\frac{1}{dz_i} + \frac{1}{dz_{i-1}}} \tag{36}$$

dz_{i-1} and dz_i are the thicknesses of the (i-1)-th and i-th atmospheric layers. With this simplification, the system can be solved locally for each atmospheric layer.

The system could be solved numerically as such by use of an iteration process. However, this could be the source of numerical difficulties and considering the range of very distinct configurations that are to be encountered in GCM simulations, we preferred a simplified algorithm. This algorithm is strictly valid in the limit case of strongly stratified atmospheres and proved accurate enough for most configurations.

The simplified algorithm is described hereafter with the convention that all variable indexed 0 are variables at time t and all non indexed variables are unknowns a time $t + dt$:

i) M is computed as the solution of Eq. 33 under the assumptions that $S_M G_M$ and $S_H G_H$ are independent of q :

$$S_{M,0} G_{M,0} \frac{M^2}{M_0^2} + S_{H,0} G_{H,0} - \frac{1}{B_1} = 0 \tag{37}$$

ii) q is computed from the knowledge of M with Eq. 35 under the assumption that $S_M G_M$ is proportional to q^2 :

$$\frac{S_{M,0}}{q_0^2} q^3 l M = F \tag{38}$$

This algorithm requires no iteration and is very robust. It is strictly valid in the limit case of strongly stratified atmospheres which is typical of Martian night conditions. It is indeed easy to observe that $S_M G_M$, $S_H G_H$ and $\frac{S_H}{q^2}$are asymptotic functions of q :

$$\lim_{q \to 0} S_M G_M = \frac{3.09}{212.} \frac{M^2}{\frac{g}{\theta_0} \frac{\partial \theta}{\partial z}} \tag{39}$$

$$\lim_{q \to 0} S_H G_H = -\frac{0.494}{34.7} \tag{40}$$

and

$$\lim_{q \to 0} \frac{S_H}{q^2} = \frac{0.494}{34.7} \frac{1}{l^2 \frac{g}{\theta_0} \frac{\partial \theta}{\partial z}} \tag{41}$$

Although the simplified algorithm is not valid for non strongly stratified configurations, it appeared to give reasonable results under the assumption $\frac{\partial \theta}{\partial z} = 0$ that can be made for most Martian day conditions when convective adjustment mixes the atmosphere until uniform potential temperatures. This assumptions leads to $G_H = 0$ and therefore S_M is constant : $S_M = 0.393$. Eq. 33 becomes

$$B_1 S_M l^2 M^2 = q^2 \tag{42}$$

which can be reported in Eq. 35 to give :

$$q^2 = \sqrt{\frac{B_1}{S_M}} F \tag{43}$$

It can be noted that the simplified algorithm leads to a similar solution under the same assumptions. Eq. 37 gives :

$$M^2 = \frac{q_0^2}{S_M l^2 B_1} \tag{44}$$

and Eq. 38 leads to :

$$\frac{q^3}{q_0} = \sqrt{\frac{B_1}{S_M}} F \tag{45}$$

which is comparable to Eq. 43 provided that the conditions do not vary to much from one time step to the other.

5.5 Typical results

In Figure 10 in situ high frequency measurements obtained by the Viking Lander 1 in spring are compared with 1D model results. These measurements were made at 1.6 m above the surface whereas the center of the first GCM layer is around 4 m. This altitude difference does not allow an exact comparison, especially for the

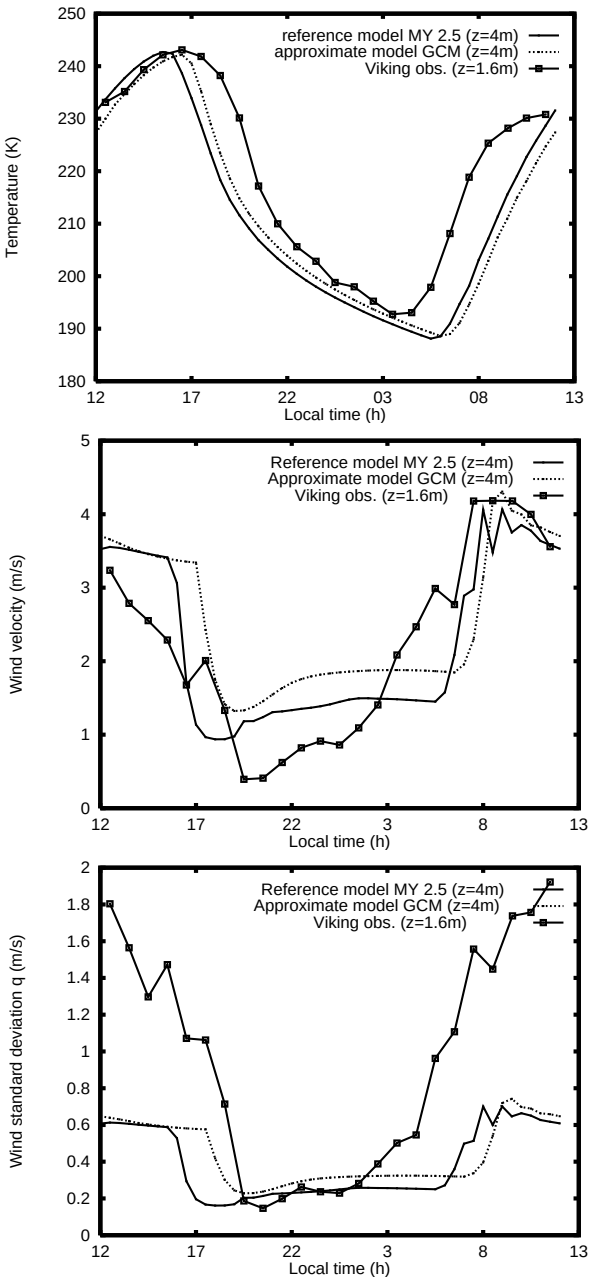

Figure 10: A comparison of Viking Lander 1 observations of temperature, wind mean velocity and standard deviation q measured 1.6 m above the surface during sol 554 ($L_s = 45^o$) with results from the 1D boundary layer scheme at about 4 m. The model parameters are the same than for 10. The high frequency Viking data were kindly provided by J.E. Tillman, Viking Computer Facility.

wind at night when stratification is very strong immediately above the surface. Another major source of differences between model and observations is the convective adjustment which is not associated with any TKE increase in the present model. This explains the low TKE values simulated during the day, whereas Viking actually recorded wind fluctuations as high as 2m s^{-1}. This difference does not alter the mean wind predictions significantly, however. The mean wind velocities predicted by the combined boundary layer/convection schemes seem to match closely the observations. More comparisons concerning the simulation of variations in wind direction with the full 3-D GCM can be found in Lewis et al. (1999). Altogether, it can be concluded that the proposed turbulence model allows economical and realistic estimations of most surface environmental variables and their diurnal evolution.

6 Convection

As in the original LMD model (Hourdin 1993), we use a standard convective adjustment scheme which rapidly mixes heat and momentum in convectively unstable layers. If an unstable profile ($\frac{\partial \theta}{\partial z} < 0$) is produced by the model, an adiabatic profile is immediately restored with a simple energy conserving scheme. If the resulting temperature profile is unstable at its upper or lower limit this mechanism is instantaneously extended in such a way that the final profile is entirely stable.

This convective adjustment is in fact achieved in a real atmosphere by parcel exchange through vertical convective motions. These motions not only transport energy but also momentum. The intensity of the momentum exchange is linked to the mass fluxs involved in the convection, which cannot be estimated in such a simple model. The best one can do is to compute an estimate of the instability of the atmosphere from the relative enthalpy exchange necessary to restore the adiabatic profile $\bar{\theta}$ from the original profile θ

$$\alpha = \int \left| \theta - \bar{\theta} \right| \rho dz \int \theta \rho dz \tag{46}$$

When $\alpha < 1$ (this condition is always verified in the simulations) the angular momentum is entirely mixed on a fraction α of the mesh. This rather arbitrary choice is qualitatively acceptable in the sense that a larger instability will produce a larger momentum mixing.

7 Representation of Sub-Grid Scale Orography

7.1 Introduction

The orography used in the GCM is smoothed to the horizontal resolution of the model i.e. variations of orography below the grid scale are effectively ignored. These sub-grid scale variations can, however, have a significant impact on the circulation of the atmosphere, so their effect must be parametrised in some way. More specifically the sub-grid scale mountains can influence the model scale flow in two ways, (a) by producing a form drag on the flow at low levels, and (b) by exciting internal gravity waves which can propagate in the vertical, break, and decelerate the flow far away from the mountains themselves. We have chosen to parametrise these two effects using, for (a), the low level drag scheme of (Lott and Miller, 1997) and for (b) the gravity wave drag scheme of (Miller et al., 1989) and (Baines and Palmer, 1990) which was developed from the (Palmer et al., 1986) scheme. Both these schemes are state of the art and are in current operational use at the European Centre for Medium Range Weather Forecasting.

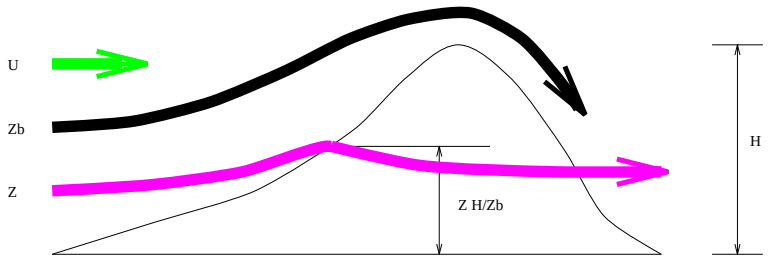

Figure 11: Schematic representation of the low level flow behaviour in sub-grid scale orographic drag parametrisation scheme.

7.2 Low Level Drag Parametrisation

A complete account of the low level drag parametrisation scheme, together with its validation against observations and an account of its performance in the ECMWF forecast model, can be found in (Lott and Miller, 1997). The details of the scheme are reproduced here for completeness.

We define the non-dimensional height of a single mountain, H_N, as

$$H_N = \frac{N H}{|U|} \tag{47}$$

where H is the maximum height of the mountain, U is the speed of the wind incident on the mountain and N is the Brunt-Viäsälä frequency.

At small H_N all the air flows over the mountain and gravity waves are generated (see section 7.3). There is no low level flow drag in this case. At large H_N part of the low level air flow goes around the mountain producing a drag on the low level flow. Figure 11 shows a schematic of the flow at large H_N.

The drag, D, on the low level flow can be written as

$$D(z) = -\rho\, C_d\, l(z)\, \frac{u|u|}{2} \tag{48}$$

where ρ is the density, $l(z)$ is a length scale based on the horizontal scale of the intersection of the mountain with the incident flow, and C_d is a drag coefficient of order unity. For an elliptical mountain, i.e.

$$h = \frac{h}{1 + \dfrac{x^2}{a^2} + \dfrac{y^2}{b^2}} \;:\; b > a \tag{49}$$

then

$$l(z) = 2b\sqrt{\frac{Z_b - z}{z}} \tag{50}$$

where Z_b is the upstream elevation of the lowest isentrope that goes over the mountain (see fig. 11). Z_b can be written as

$$Z_b = H\frac{(H_N - H_{NC})}{H_N} \tag{51}$$

where H_{NC} is a critical non-dimensional mountain height of order unity.

In a GCM grid box there is often more than one mountain and we must take account of this. At a given altitude, z, the intersection between the mountains and the model layer approximates to an ellipsoid of eccentricity

$$(a', b') = (a, b)\sqrt{\frac{Z_b - z}{z + \mu}} \tag{52}$$

where μ is the standard deviation of the sub-grid scale orography (see section 7.4 and fig. 13). Then $l(z)$ can be written approximately as

$$l(z) \;=\; 2\max(b\cos\psi, a\sin\psi)\sqrt{\frac{Z_b - z}{z+\mu}} \tag{53}$$

where ψ is the angle between the incident flow and the normal ridge direction θ (see section 7.4 and fig. 15). We note that if L is the width of the grid box, then for $\psi = 0$ there are $L/2a$ ridges in the box and for $\psi = \pi/2$ there are $L/2b$ ridges in the box. Hence

$$l(z) \;=\; \frac{L^2}{2}\sqrt{\frac{Z_b - z}{z+\mu}}\max\left(\frac{\cos\psi}{a}, \frac{\sin\psi}{b}\right). \tag{54}$$

If σ is the anisotropy of the orography and γ is the slope (see section 7.4 and figs. 16 and 14) we note that $a \approx \mu/\sigma$ and $a/b \approx \gamma$ hence the model low level drag is

$$D(z) \;=\; -C_d\max(2 - \frac{1}{r}, 0)\rho\frac{\sigma}{2\mu}\sqrt{\frac{Z_b - z}{z+\mu}}\max\left(\frac{\cos\psi}{a}, \frac{\sin\psi}{b}\right)\frac{U|U|}{2} \tag{55}$$

where

$$r \;=\; \frac{\cos^2\psi + \gamma\sin^2\psi}{\gamma\cos^2\psi + \sin^2\psi} \tag{56}$$

For convenience, and for consistency with the gravity wave drag scheme (section 7.3) we substitute the function $B\cos^2\psi + C\sin^2\psi$, ($B$ and C are defined in section 7.3) for the expression $\max\left(\frac{\cos\psi}{a}, \frac{\sin\psi}{b}\right)$. In the GCM the term $D(z)$ is evaluated quasi-implicitly in ensure numerical stability.

The tunable parameters in the scheme are the critical non-dimensional mountain height, H_{NC}, and the drag coefficient, C_d.

7.3 Gravity Wave Drag

Full details of the scheme are given in (Lott and Miller, 1997), (Miller et al., 1989), (Baines and Palmer, 1990) and (Palmer et al., 1986) but the essentials are reproduced here for completeness. It is common in parametrising gravity wave drag to assume a single gravity wave, with some characteristic wavelength, that propagates from the surface of the model only in the vertical plane. Schemes that represent ensembles of gravity wave schemes are computationally very expensive and, as yet, little tested in terrestrial climate models.

The vector surface stress induced by a single gravity wave generated by a single elliptical mountain, of the form given by equation (49), can be written as (Phillips, 1984,)

$$\tau \;=\; \rho\, U\, N\, H^2\, b\, G\, (B\cos^2\psi + C\sin^2\psi, (B - C)\sin\psi\cos\psi) \tag{57}$$

where $B = 1 - 0.18\gamma - 0.04\gamma^2$, $C = 0.48\gamma + 0.3\gamma^2$, G is a constant of order unity and all the other symbols are as defined in section 7.2. Summing over all mountains in the grid box the model gravity wave stress becomes

$$\tau \;=\; \rho\, U\, N\, \mu\, \sigma\, G\, (B\cos^2\psi + C\sin^2\psi, (B - C)\sin\psi\cos\psi). \tag{58}$$

We now consider what happens when the gravity wave propagates vertically. We assume that the stress at any level is parallel to the surface stress and can be written

$$\tau \;=\; |\tau| \;=\; \kappa\,\rho\, U\, N\, \delta h^2 \tag{59}$$

where $\kappa = \mu\sigma G|(B\cos^2\psi + C\sin^2\psi, (B-C)\sin\psi\cos\psi)|$ and δh can be thought of as the vertical isentropic displacement induced by the propagating gravity wave. We then judge the effect of the wave on the mean flow by calculating the minimum Richardson number attainable i.e. the Richardson number that is 'felt by the gravity wave'.

$$Ri_{min} = Ri\frac{1-\frac{N\,\delta h}{U}}{\left(1+Ri^{1/2}\,\frac{N\,\delta h}{U}\right)^2}. \tag{60}$$

Following (Lindzen, 1981) the saturation hypothesis is employed. When Ri_{min} is greater than some critical value, Ri_c, the stress remains constant with height, the gravity wave continues to propagate vertically and Ri_{min} is evaluated at the next model level. This is repeated until Ri_{min} drops below the critical value, Ri_c, and the wave is deemed to have broken. Then a new value for the isentropic displacement, δh, and hence a new value for the stress, is calculated in order to keep $Ri_{min} = Ri_c$. The whole process is repeated until the top of the model is reached and the stress is assumed to be zero i.e. the waves are assumed to be dissipated somewhere in the atmosphere. The tendencies are calculated from the vertical derivative of the stress profile. A schematic diagram of the gravity wave drag algorithm is shown in fig. 12.

The scheme represents stationary wave critical level absorption, as when the component of the wind in the direction of the surface stress approaches zero the Richardson number becomes very large causing the wave amplitude to become very small. The wave is thus absorbed at the critical level and the stress set to zero above the critical line.

The tunable parameters for the scheme are G, which multiplies the expression for the gravity wave surface stress, and Ri_c, the critical Richardson number.

.

7.4 Sub-grid Scale Orographic Parameters

As has already been indicated (sections 7.2 and 7.3), the sub-grid scale orography is specified by 4 parameters; the standard deviation within the grid box, μ, the anisotropy, γ, the angle of the principal axes of the orography, θ, and the slope parameter, σ (Lott and Miller, 1997; Baines and Palmer, 1990,). They are defined as follows. Let $h(x,y)$ be the orography within the grid box defined at N points and $\bar{h}$ be the mean orography, then

$$\mu = \frac{\sqrt{\sum(h-\bar{h})^2}}{N} \tag{61}$$

$$\theta = \frac{1}{2}\arctan\left(\frac{L}{M}\right) \tag{62}$$

where

$$M = \overline{\frac{\partial h}{\partial x}\frac{\partial h}{\partial u}} \tag{63}$$

and

$$L = \frac{1}{2}\left(\left(\frac{\partial h}{\partial x}\right)^2 - \left(\frac{\partial h}{\partial y}\right)^2\right). \tag{64}$$

The anisotropy is

$$\gamma = \sqrt{\left(\frac{\partial h}{\partial y'}\right)^2 \Big/ \left(\frac{\partial h}{\partial x'}\right)^2} \tag{65}$$

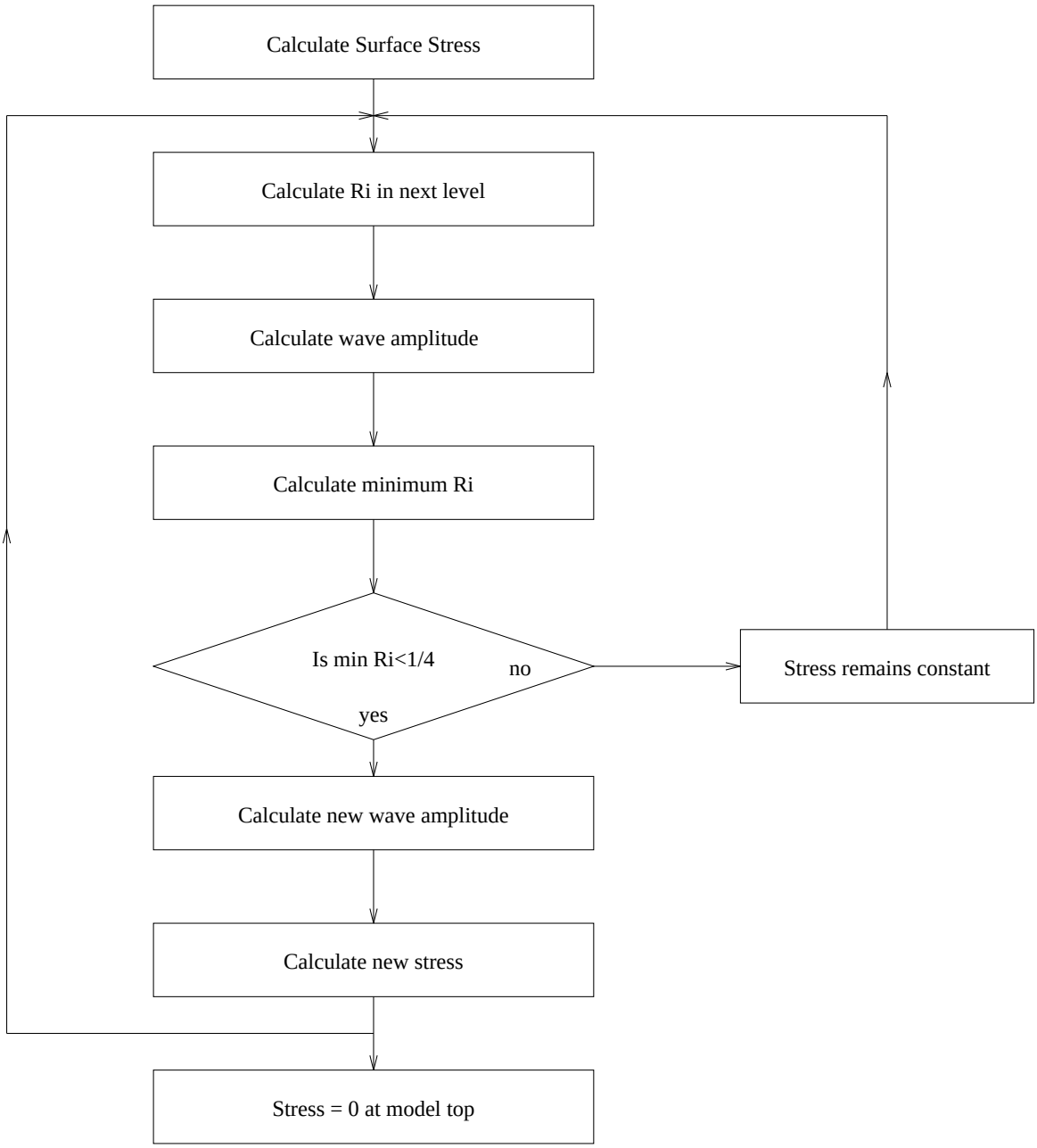

Figure 12: A schematic diagram of the gravity wave drag algorithm.

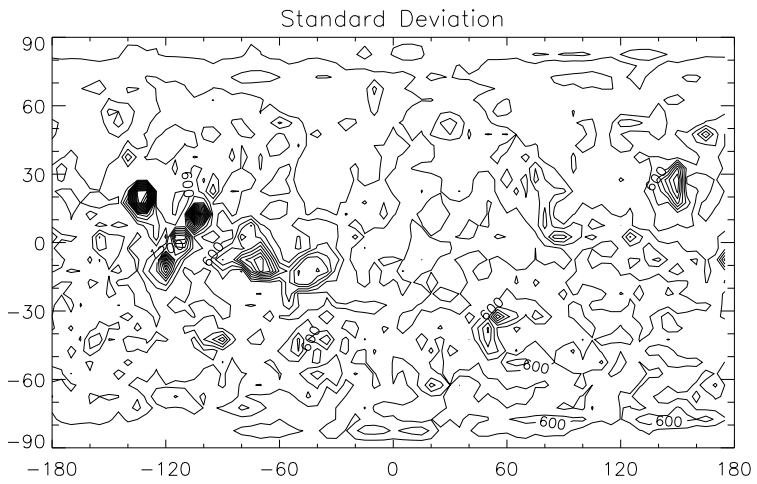

Figure 13: The sub-grid scale orographic standard deviation, μ. The contour interval is $300m$.

where

$$x' = x\cos\theta + y\sin\theta \tag{66}$$

and

$$y' = y\cos\theta - x\sin\theta, \tag{67}$$

and the slope parameter, σ, is defined by

$$\sigma^2 = \overline{\left(\frac{\partial h}{\partial x'}\right)^2} \tag{68}$$

These parameters have been calculated from the Mars Digital Topographic Map (Wu, 1981, DTM,) at $1^\circ \times 1^\circ$ degrees resolution and are shown in figures 13-16.

8 CO_2 condensation-sublimation Scheme

8.1 Physics of the condensation-sublimation process

The condensation and sublimation of carbon dioxide on the ground is primarily controlled by relatively simple physical processes. When the surface temperature falls below the condensation temperature, CO_2 condenses, releasing the latent heat required to keep the solid-gas interface at the condensation temperature. Conversely, when CO_2 ice is heated, it partially sublimes to keep its temperature at the frost point temperature.

In the atmosphere, things are, in theory, more complex. The condensation of a gas involves various microphysical processes: supersaturation, nucleation, crystal growth, sedimentation, etc... On Earth, such processes control the formation of the clouds. They have to be taken into account in General Circulation Models. On Mars, what should we take into account ? First, temperatures colder than the solid-gas equilibrium temperature (supersaturation) may be required to form (nucleation) the condensed particles from the vapor phase. However, on Mars, nucleation is probably facilitated by the presence of airborne dust particles which can serve as condensation nuclei (heterogeneous nucleation). In such conditions, preliminary studies conducted with microphysical models by Wood *et al.* (1996) and Stansberry

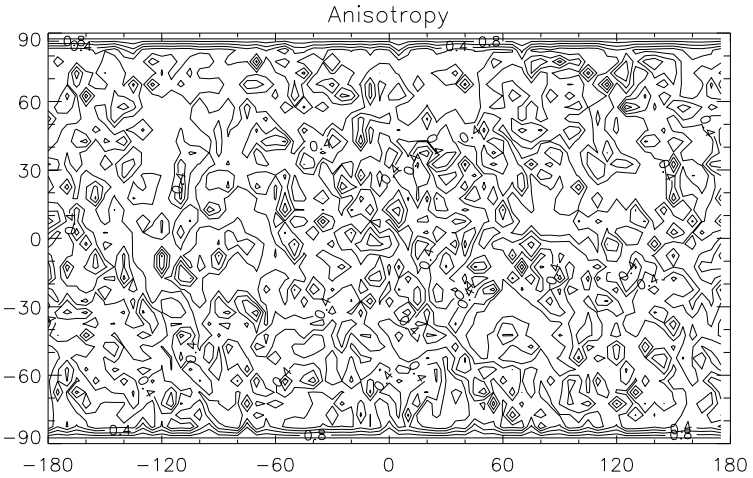

Figure 14: The sub-grid scale orographic anisotropy parameter, γ. The contour interval is 0.2.

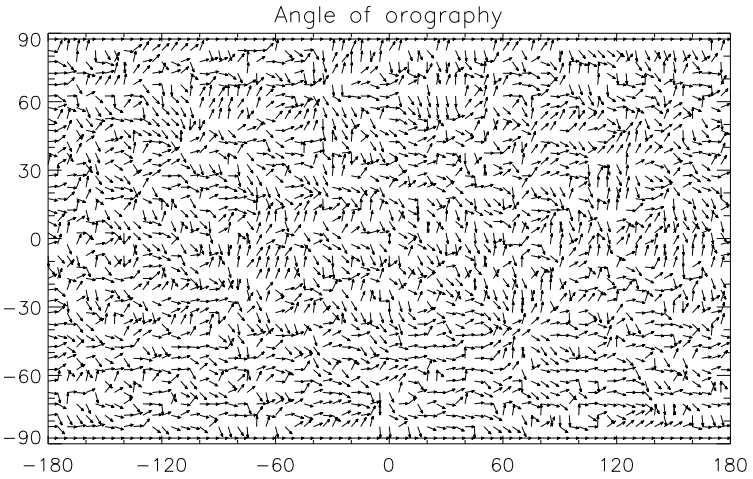

Figure 15: The angle of the principal axes of the sub-grid scale orography, θ, indicated by vectors.

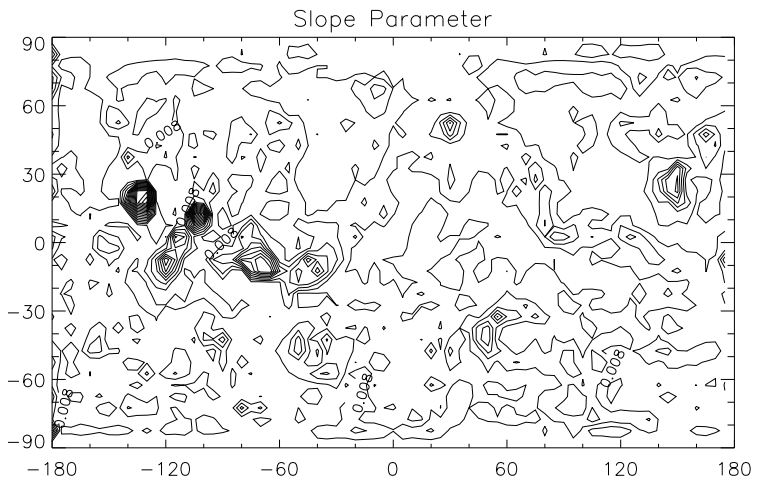

Figure 16: The sub-grid scale orographic slope parameter, σ. The contour interval is 0.004.

et al. (1995) indicate that, in terms of temperature, the supersaturation required to form CO_2 ice particles in a CO_2 atmosphere is negligible. Thus, we assume that condensation occurs as soon as the temperature reaches the frost point.

For a given condensation rate, the number of particles, their sizes and their rates of sedimentation depend upon numerous and poorly known parameters such as the number of nuclei available, or the finite rate at which CO_2 molecules can be incorporated into the crystal lattice. It must be noted that CO_2 crystals growing in a CO_2 atmosphere present a totally different regime than water ice clouds particles on Earth (Rossow 1978). The growth of water clouds particles on Earth is limited by both the diffusion of water vapor though air and the thermal diffusion of latent heat of condensation away from the particle, whereas the mass diffusion effect is entirely absent in CO_2 ice clouds. Thus for equal supersaturations, CO_2 ice cloud particles should grow faster than the corresponding water ice particles (Pierrehumbert and Erlick 1997). In the model, until more data and model results become available, we have made the following assumption : after condensing at a given level, the CO_2 ice falls through the atmospheric layers located below it down to the ground within a model timestep. In reality, the ice particles fall more slowly and may be horizontally advected by the wind. However, since the atmosphere keeps condensing (the atmosphere is usually supersaturated down to the surface), and this preferentially on the CO_2 ice already formed, the particle size should readily increase. Because the sedimentation velocity is proportional to the square of the particles radius (Stokes' law), it is unlikely that the CO_2 ice may be transported over significant distances. For instance, Wood *et al.* (1996) estimated that the particle size near the surface should be at least 100 μm, corresponding to a sedimentation velocity larger than 1.4 m s^{-1} (see Table 1, Forget *et al.* 1995). Since the radiative properties of the clouds are taken into account independently (see below), our assumption should not affect the condensation rate on the ground and in the atmosphere. Therefore, the calculation of the condensation rate in the atmosphere is reduced to an of energy and mass budget, similar to the ground case. In the original version of the general circulation model, the CO_2 ice condensing in the atmosphere was simply included in the mass budget of the surface, without taking into account its altitude, its initial temperature and the layers through which it fell. We have since found that this approximation can lead to errors of

several percent on the total amount of CO_2 condensed seasonally in the polar caps. The error on the part condensing in the atmosphere was especially large. Thus, we have re-addressed this issue more carefully, with particular attention to mass and energy balances. We now allow for the possible sublimation of sedimenting CO_2 ice particles in warmer atmospheric layers as they descend to the ground. Minor components of the energy budget are included (e.g. the release of potential energy by CO_2 ice particles during their fall, and the heat consumption to warm the particles as the CO_2 frost temperature increases with the local pressure). Also, we have included a correction to account for the mass, heat and momentum redistribution between the model layers due to condensation (see appendix). Last, the boundary layer scheme has been modified so that the turbulent atmospheric mixing takes into account the fact that the atmosphere can never be colder than the CO_2 frost point.

8.2 Numerical scheme

Condensation and sublimation in the atmosphere. The model atmosphere consist of N layers. In each layer, at each computational timestep, the CO_2 gas condenses when the temperature T^* predicted from the dynamical and radiative cooling rates is below the condensation temperature[1] Tc. The temperature T is then set to Tc. The corresponding enthalpy deficit must be balanced by the CO_2 condensation. Condensation is computed from top to bottom. In the upper level N of the model, this yields :

$$\delta m_N = \frac{c_p M_N}{L}(Tc_N - T_N^*) \tag{70}$$

With δm_N the mass of ice that has condensed (>0 when condensing), M_N the layer mass, c_p the specific heat at constant pressure (735.9 J kg^{-1} K^{-1} on Mars) and L the latent heat of CO_2 (5.9 10^5 J kg^{-1}). Below this level, the fact that the atmosphere might have condensed in the layers above must be taken into account :

$$\delta m_l = \frac{c_p M_l}{L}(Tc_l - T_l^*) - \frac{1}{L}[g(z_{l+1} - z_l) + c_{ice}(Tc_{l+1} - Tc_l)] \sum_{k=l+1}^{N} \delta m_k \tag{71}$$

with z_l the altitude in the middle of layer l ; g the acceleration of gravity ; c_{ice} the specific heat of CO_2 ice (349+4.8T J kg^{-1} K^{-1}, with 73 K< T < 200 K, from Washburn 1948); and $\sum_{k=l+1}^{N} \delta m_k$ the amount of ice that condensed in the layers above, falling from layer l+1. The term $[g(z_{l+1} - z_l) \sum_{k=l+1}^{N} \delta m_k]$ corresponds to the potential energy released by this amount of ice falling from layer l+1 (aerodynamical friction). The term $[c_{ice}(Tc_{l+1} - Tc_l) \sum_{k=l+1}^{N} \delta m_k]$ corresponds to the energy used to heat the mass $\sum_{k=l+1}^{N} \delta m_k$ from the temperature Tc_{l+1} to Tc_l. These two terms are not negligible: 1 kg of ice condensed at z = 10 km (about one atmospheric scale height) would release gz = 3.73 10^4 J and would consume $c_{ice}(Tc(z) - Tc(0)) \simeq -10^4$ J, respectively 6.3 and 1.7% of the latent heat initially released (5.9 10^5 J).

The ice condensed in the atmosphere can resublime during its descent if it encounters warm layer with $T_l > Tc_l$. Equation 71 then remains valid and the amount

[1] The condensation temperature Tc is computed using the Clausius-Clapeyron relation for perfect gas (Hourdin 1995). Assuming that the latent heat of sublimation L is independent of temperature, the vapor pressure curve reduces to

$$\ln(p/p_0) = \frac{L}{R}\left(\frac{1}{T_0} - \frac{1}{T_{CO_2}}\right) \tag{69}$$

(where R is the gas constant and T_0 is the condensation temperature corresponding to the pressure chosen as a reference, here p_0 = 1 mbar). $L = 5.9 \times 10^5$ J kg^{-1} and T_0 = 136.3 K are fixed in the range of experimental values (James et al., 1992, e.g.,).

$\delta m_l < 0$ is sublimed. However, if all the ice falling from the layers above sublimes in layer l (case when equation 71 predicts: $-\delta m_l > \sum_{k=l+1}^{N} \delta m_k$), we set $\delta m_l = -\sum_{k=l+1}^{N} \delta m_k$ and the layer temperature T_l is then given by:

$$T_l = T_l^* + \frac{1}{c_p M_l}[-L + g(z_{l+1} - z_l) + c_{ice}(Tc_{l+1} - Tc_l)] \sum_{k=l+1}^{N} \delta m_k \qquad (72)$$

Condensation and sublimation on the ground. Condensation on the ground is controlled by the same kind of equation as for atmospheric condensation. Equation 71 remains valid with $l = 0$ and replacing $c_p M_l$ by $c_s A$, with A the area of the grid mesh and c_s the surface heat capacity (in J m^{-2} K^{-1}). At each timestep, in the model, the mass $\sum_{k=0}^{N} \delta m_k$ is added to the amount of ice on the ground m_0. We set $T_0 = Tc_0$, unless the ground ice completly sublimes (case when $-\delta m_0 > m_0 + \sum_{k=1}^{N} \delta m_k$ is predicted). We then set $\delta m_0 = -m_0 - \sum_{k=1}^{N} \delta m_k$ and the new surface temperature is expressed as:

$$T_0 = T_0^* - \frac{L}{C_s A} m_0 - \frac{1}{C_s A}[L - gz_1 - c_{ice}(Tc_1 - Tc_0)] \sum_{k=1}^{N} \delta m_k \qquad (73)$$

Energy and mass balance in vertical coordinates σ=p/p_0. The loss of atmospheric mass due to condensation (or conversely the gain due to sublimation) is taken into account by modifying the surface pressure at each timestep by :

$$\delta p_0 = -\frac{g}{A} \sum_{k=0}^{N} \delta m_k \qquad (74)$$

This ensures the conservation of the total mass of CO_2 (caps + atmosphere). However, in each layer, the condensation-sublimation induces some transfers of mass, heat and momentum which require a specific treatment. In particular, like in most GCMs, the layers in our model are defined by fixed coordinates $\sigma = p/p_0$. The changes in p_0 due to the CO_2 condensation-sublimation induce "artificial" movements of the σ levels in the atmosphere. This must be reflected in the temperature and wind fields. In a grid mesh of area A, let's consider a layer l delimited by the levels $\sigma_{l-\frac{1}{2}}$ and $\sigma_{l+\frac{1}{2}}$. At each timestep, its mass $M_l = \frac{A}{g}(\sigma_{l-\frac{1}{2}} - \sigma_{l+\frac{1}{2}})p_0$ varies because of the global variation of p_0. Such a variation is associated with transfers of mass between the layers (on which one must add the sink corresponding to the local condensation $-\delta m_l$). The local mass balance may be written :

$$\delta M_l = \frac{A}{g}(\sigma_{l-\frac{1}{2}} - \sigma_{l+\frac{1}{2}})\delta p_0 = W_{l-\frac{1}{2}} - W_{l+\frac{1}{2}} - \delta m_l \qquad (75)$$

where $W_{l-\frac{1}{2}}$ is the air mass (kg) "transfered" through the level $\sigma_{l-\frac{1}{2}}$ (> 0 when up) during the timestep. Equations 74 and 75 may be combined to yield a recursive formula on W :

$$W_{l+\frac{1}{2}} = W_{l-\frac{1}{2}} - \delta m_l + (\sigma_{l-\frac{1}{2}} - \sigma_{l+\frac{1}{2}}) \sum_{k=0}^{N} \delta m_k \qquad (76)$$

with:

$$W_{\frac{1}{2}} = -\delta m_0 \qquad (77)$$

The knowledge of W can then be used to compute the exchange of heat and momentum between the layers. For $c_p T$ (enthalpy), the local heat balance can be written :

$$\delta(M_l T_l) = W_{l-\frac{1}{2}} \overline{T}_{l-\frac{1}{2}} - W_{l+\frac{1}{2}} \overline{T}_{l+\frac{1}{2}} - \delta m_l \; Tc_l \tag{78}$$

with $\overline{T}_{l-\frac{1}{2}}$ the mean temperature of the gas transported through the $\sigma_{l-\frac{1}{2}}$ interface. Various operators have been suggested in the litterature to calculate $\overline{T}_{l-\frac{1}{2}}$. Indeed, this process is similar to a classical transport process. A simple arithmetic average ($\overline{T}_{l-\frac{1}{2}} = (T_l + T_{l-1})/2$) could have been used for instance, but we found that, because of the thiness of the layers near the surface in our model, more accurate results were obtained with a higher order scheme. We used the "Van-Leer I" finite volume transport scheme (Van-Leer 1977, Hourdin and Armengaud 1997), with, on the ground, $\overline{T}_{\frac{1}{2}} = T_0$.

Separately, one can also write :

$$\delta(M_l T_l) \simeq M_l \delta T_l + T_l \delta M_l \tag{79}$$

with δT_l a correction to be applied at every timestep in each layer after the CO_2 condensation or sublimation. Eqs 78 and 79 may be combined to obtain δT_l

$$\delta T_l = \frac{1}{M_l}[W_{l-\frac{1}{2}}(\overline{T}_{l-\frac{1}{2}} - T_l) - W_{l+\frac{1}{2}}(\overline{T}_{l+\frac{1}{2}} - T_l) + \delta m_l (Tc_l - T_l)] \tag{80}$$

The first two terms, with $W_{l-\frac{1}{2}}$ and $W_{l+\frac{1}{2}}$, correspond to the re-arrangement of the temperatures over the entire column due to the pressure variations in σ coordinates. The last term $\delta m_l (Tc_l - T_l)$ is usually equal to zero when CO_2 condenses or partially sublimes since we then have $Tc_l = T_l$. However, when the CO_2 totally sublimes (case of the equation 72), it becomes a cooling term accounting for the mixing of the newly sublimed mass $-\delta m_l$ with the rest of the layer at $T_l > Tc_l$.

In the lower layer, equation 80 can be rewritten:

$$\delta T_1 = \frac{1}{M_1}[-\delta m_0 (T_0 - T_1) - W_{1+\frac{1}{2}}(\overline{T}_{1+\frac{1}{2}} - T_1) + \delta m_1 (Tc_1 - T_1)] \tag{81}$$

The term $\delta m_0 (T_0 - T_1)$ corresponds to the condensation-sublimation flux from the ground. This term can be considerable during the sublimation phase in spring and summer, when the temperature difference between the lower atmosphere and the ground reaches 50 K. The cooling of the first layer by the newly sublimed CO_2 is then comparable to a loss of energy $c_p(T_0 - T_1)/L \simeq 6\%$ of the latent heat initially required.

Similarly, the momentum distribution must be re-arranged, although condensation and sublimation cannot be considered as sinks or sources of momentum. For a wind component v, we shall simply write:

$$\delta v_l = \frac{1}{M_l}[W_{l-\frac{1}{2}}(\overline{v}_{l-\frac{1}{2}} - v_l) - W_{l+\frac{1}{2}}(\overline{v}_{l+\frac{1}{2}} - v_l)] \tag{82}$$

with, on the ground, $\overline{v}_{\frac{1}{2}} = v_1 \delta m_0 / M_1$ if $\delta m_0 > 0$ and $\overline{v}_{\frac{1}{2}} = 0$ if $\delta m_0 < 0$ (the velocity of the CO_2 gas that has just sublimed is zero).

9 The "CO_2 snow scheme: Modeling the impact of the CO_2 clouds and fresh snow on the radiative budget

9.1 Introduction: Clouds or snow?

The thermal Infrared instruments aboard Viking and Mariner 9 have shown that the CO_2 condensation rate was strongly reduced by some processes locally decreasing

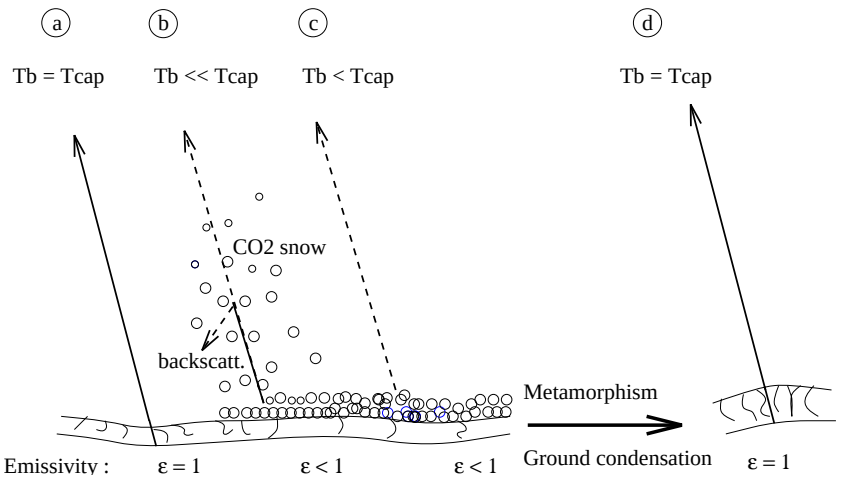

Figure 17: Schematic representation of the CO_2 snow fall scenario parametrized in the model to simulate the "low emission zones" observed in the polar night (see *Forget et al.*, 1995, 1996). (a) outside of the low emission zones, the cap emissivity ϵ is close to one; (b) During a snow fall, the airborne CO_2 ice particles scatter the thermal radiation back to the ground, and, once on the ground decrease the surface emissivity ϵ; (c) After the end of the snow fall, the emissivity ϵ remains below one until metamorphism and ground condensation increase the CO_2 ice grain size, and thus ϵ; (d) Ultimately, the ice layer become nonporous and transparent, and the infrared radiation emitted by the ground can radiate through with $\epsilon \simeq 1$

the infrared emission toward space (Forget et al., 1996). The location and brightness temperatures of these areas, also called "low emission zones", sometimes varied on time scales of days [*Kieffer et al.*, 1977]. Forget et al. (1995) used a combination of radiative transfer modeling and infrared data analysis to show that the low brightness temperatures were likely to be created by the radiative properties of CO_2 ice particle when these particles where formed up in the atmosphere rather than directly on the ground (Fig. 17). In that case, the infrared emission is decreased because the CO_2 snow grains can be efficient scatterers at infrared wavelengths, whether they are airborne (precipitating clouds) or on the ground (fresh snow).

The amount of CO_2 condensing in the atmosphere can be estimated with the GCM. Unfortunately, not much is known about the CO_2 clouds microphysics and even less about the processes which control the metamorphism of the CO_2 snow at the surface. Consequently, linking the CO_2 condensation rate with the actual radiative effect of the cloud and snow on the basis of physical considerations is not straightforward. Thus we make several assumptions. First, we have chosen not to distinguish between airborne snow flakes and surface snow. Indeed, the available observations do not permit us to distinguish between these two cases, and it is not known wether the reduction of the infrared fluxes emitted by the polar regions is primarily due to the snow in the air or on the ground. In fact, both surface snow (by reducing the surface emissivity) and clouds (by backscattering the infrared radiation) decrease the net infrared radiative fluxes at the surface and at the top of the atmosphere. For the ground, and for the atmosphere above the top of the scattering clouds, the radiative budget is the same in both cases. In the model, the radiative effects of CO_2 snow and clouds have therefore been parametrized by simply decreasing the surface emissivity ε. The main impact of such a simplification is to underestimate the upward and downward infared fluxes in the layers located between the surface and the top of the scattering cloud. When the atmo-

sphere is clear, this should not affect the condensation rate, since the radiation is backscattered at wavelengths which, by definition, cannot be absorbed by the CO_2 ice and gas. When the atmosphere is dust laden, our assumption might lead to an overestimate of the atmospheric cooling rate, and in turn, of the atmospheric condensation. However, only the layers located below the scattering clouds with particle radii $> 10\mu$m (and thus close to the ground) should be affected.

9.2 Variation of the snow emissivity

The surface emissivity ε in our model is thus supposed to account for the variation of the actual emissivity of the system [ground + ice + fresh snow + clouds]. ε will decrease with the accumulation of particles having condensed in the atmosphere. During a snowfall at a given time, atmospheric condensation accumulates a layer of mass m (kg m^{-2}) of scattering particles. The particle sizes in this layer are probably extremely variable, from the top of the clouds to the snow layers underneath. For our parametrization, a detailed knowledge of the vertical distribution of the particle sizes is not required since we are only concerned with the global impact of the entire layer on the radiation budget. Thus, we can assume that the size distribution in this layer can be represented by a single effective radius r. This radius probably ranges between 10 μm (the minimum size to efficiently scatter thermal radiation) and a few hundreds micrometers, consistently with microphysical considerations (Wood *et al.* 1996).

At a given wavelength, the optical depth corresponding to mass m is given by:

$$\tau = \frac{3Q_{ext}}{4\rho r} m \tag{83}$$

Where ρ is the CO_2 ice density (about 1630 kg m^{-3} at 140 K) and Q_{ext} the extinction parameter. At 20 μm, where the CO_2 ice is almost transparent, Q_{ext} should be close to the scattering parameter Q_{scat}. For particles larger than 25 μm, Q_{ext} should therefore be close to the asymptotic value 2. For particles with radii between 10 and 25 μm, according to the Mie theory, Q_{ext} may theoretically reach 4 because of resonance processes. In reality, however, the broad size distribution should decrease these effects (Hansen and Travis 1974) and we can also take $Q_{ext} \simeq 2$. The optical depth τ should thus only be a function of r and m. In S.I. units, $\tau \simeq 10^{-3}\, m/r$.

The impact of such a layer of optical depth τ on the thermal radiation can be computed with a radiative transfer model. The model employed in our calculations is basically the same as that used by Forget *et al.* (1995) and described in more detail by Toon *et al.* (1989) and Pollack *et al.* (1993b). This algorithm is based on the two-stream, hemispheric mean, source function solution to the equation of radiative transfer and allows for the emission angle of the observations. The single-scattering calculation follows Mie theory. The results, presented in Fig. 18, show that at a given wavelength, the decrease of infrared flux due to backscattering depends upon the particle radius and the amount of water ice mixed with the CO_2 ice (such water ice particles are thought to be present at least in the northern hemisphere). The vertical axis in Fig. 18 corresponds to the emissivity ε of the system ground + scattering layer that we are parameterizing. In most realistic cases, ε is well approximated by $\varepsilon = (1 + \alpha\tau)^{-1/3}$ with $0.15 < \alpha < 1.5$, $\alpha = 0.45$ being an appropriate mean value. Using $\tau \simeq 10^{-3}\, m/r$ yields :

$$\varepsilon = (1 + 10^{-3}\, \frac{\alpha}{r} m)^{-1/3} \tag{84}$$

Differentiation with respect to time gives the equation governing the decrease of

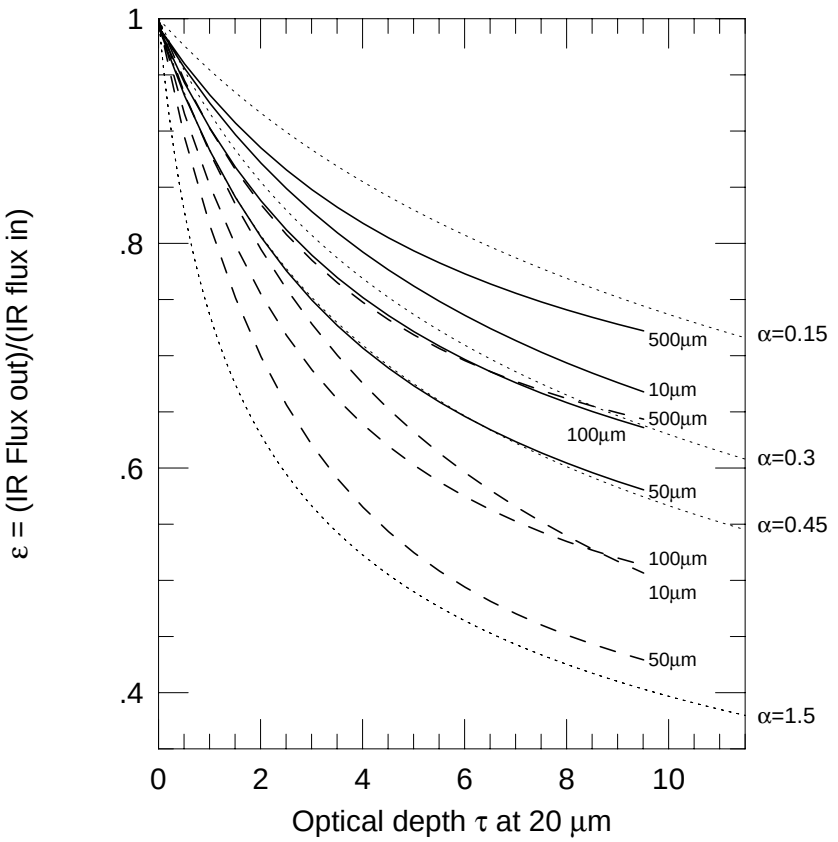

Figure 18: Reduction of the outgoing infrared flux due to a layer of CO_2 ice particles of radius 10, 50, 100 and 500 μm, and of various optical depths. The particles and surface temperature is 145 K. CO_2 ice is pure (dashed lines) or mixed with 10 g.m^{-2} of water ice (solid lines). Dotted lines show examples of the curve $\varepsilon = (1+\alpha\tau)^{-1/3}$, used to fit the results of the radiative transfer model.

ε:

$$\frac{\partial \varepsilon}{\partial t} = -\frac{10^{-3}}{3}\,\varepsilon^4\,\frac{\alpha}{r}\frac{\partial m}{\partial t} \tag{85}$$

$\partial m/\partial t$ corresponds here to the atmospheric condensation rate (kg.m^{-2}.s^{-1}).

In reality, the decrease of ε due to the CO_2 snowfall is probably limited by the fact that, once on the ground, the CO_2 snow flakes progressively loose their scattering properties. Indeed, the continuing surface condensation should tend to aggregate the grains. A kind of "destructive metamorphism" may also play a role (Eluszkiewicz 1993). To simplify, we have assumed that ε was restored toward unity with a characteristic timescale $\mathcal{T}$. This timescale should be of the order of the low emission zones time scale observed by Viking, probably less than one day (Kieffer *et al.* 1977, Forget *et al.* 1995). In our model, the governing equation for the emissivity ε as a function of the condensation rate $\partial m/\partial t$ becomes :

$$\frac{\partial \varepsilon}{\partial t} = -\frac{10^{-3}}{3}\,\varepsilon^4\,\frac{\alpha}{r}\frac{\partial m}{\partial t} + \frac{1}{\mathcal{T}}(1-\varepsilon) \tag{86}$$

This parametrization depends on only two "unknown" parameters, namely $\mathcal{T}$ and r (actually α/r, but α is set to its mean value $\alpha = 0.45$, r remaining variable). Moreover, the stationary solution of equation 86 (corresponding to $\partial\varepsilon/\partial t = 0$) only involves the ratio $r/\mathcal{T}$. On average, this ratio will control the value of ε, making the model very simple.

9.3 Numerical scheme

At every timestep, $\delta\varepsilon$ is added to ε ($\varepsilon_{t+\delta t} = \varepsilon_t + \delta\varepsilon$). The atmospheric condensation rate is calculated by the model in every layer: $\frac{\partial m}{\partial t} = \sum_{k=1}^{N} \frac{\delta m_k}{\delta t}$ (with the notation of the previous section). In the GCM, the physical parametrizations timestep is of the order of 1/40 day. The equation 86 cannot be approximated directly by $\delta\varepsilon/\delta t = \partial\varepsilon/\partial t$ because δt may be too long compared to the time constant of the second term from equation 86 (Typically $[\frac{10^{-3}}{3}\,\varepsilon^3\,\frac{\alpha}{r}\sum_{k=1}^{N}\frac{\delta m_k}{\delta t}]^{-1}$). Nevertheless, if we assume that the increasing and the decreasing terms can be separated ($\delta\varepsilon = \delta\varepsilon_\uparrow + \delta\varepsilon_\downarrow$), $\delta\varepsilon_\downarrow$ can be derived from the integration of équation 85 over one timestep:

$$\varepsilon^{-3} - (\varepsilon + \delta\varepsilon_\downarrow)^{-3} = -10^{-3}\,\frac{\alpha}{r}\sum_{k=1}^{N}\frac{\delta m_k}{\delta t} \tag{87}$$

The increasing term, on the other hand, can directly be computed from the second term of equation 86 with $\frac{\delta\varepsilon_\uparrow}{\delta t} = \frac{1}{\mathcal{T}}(1-\varepsilon)$, since we should always have $\delta t << \mathcal{T}$.

At every timestep, the increment is thus given by [2] :

$$\delta\varepsilon = (\varepsilon^{-3} + 10^{-3}\,\frac{\alpha}{r}\sum_{k=1}^{N}\delta m_k)^{-1/3} - \varepsilon + \frac{\delta t}{\mathcal{T}}(1-\varepsilon) \tag{88}$$

[2] In practice, the emissivity ε_0 of the ground below the ice is lower than unity ($\varepsilon_0 = 0.95$ in the model). The actual polar cap emissivity in the model ε_m is thus given by the product $\varepsilon \times \varepsilon_0$ with ε computed following equation 86. Its governing equation is thus:

$$\frac{\partial \varepsilon_m}{\partial t} = -\frac{10^{-3}}{3}\,\frac{\varepsilon_m^4}{\varepsilon_0^3}\,\frac{\alpha}{r}\frac{\partial m}{\partial t} + \frac{1}{\mathcal{T}}(\varepsilon_0 - \varepsilon_m)$$

In the model, we shall use the integrated version:

$$\delta\varepsilon_m = [(\frac{\varepsilon_m}{\varepsilon_0})^{-3} + 10^{-3}\,\frac{\alpha}{r}\sum_{k=1}^{N}\delta m_k]^{-1/3} - \varepsilon_m + \frac{\delta t}{\mathcal{T}}(\varepsilon_0 - \varepsilon_m)$$

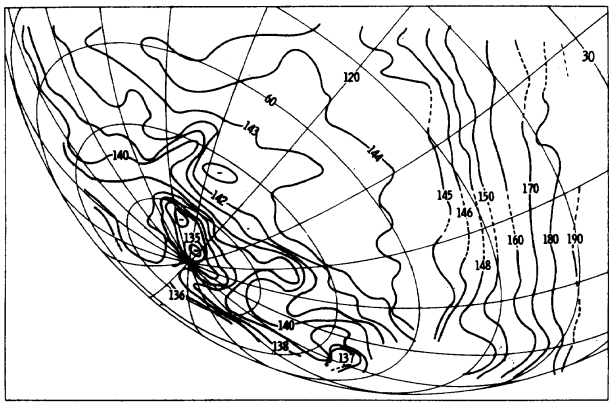

(a) Brightness temperatures observed by Viking (K)

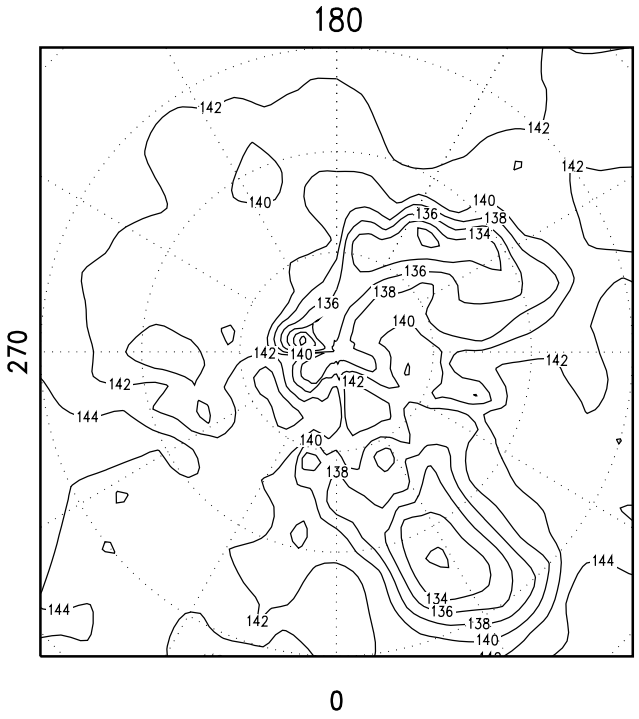

(b) Brightness temperatures simulated by the model (K)

Figure 19: Examples of spatial patterns of the 20-μm brightness temperatures (a) observed by the Viking IRTM instrument during the winter in the south polar region ($L_s = 93^o$, figure from Kieffer *et al.* 1976), and (b) simulated by the model with the parameterization of the CO_2 snow falls which are thought to locally decrease the outgoing infrared flux, thus creating low brightness temperature features. ($\tau = 0.1$, $L_s = 120^o$, figure from Forget et al. 1998b).

9.4 Typical results

Overall, without tuning the model parameters, we have been able to accurately reproduce the general behavior of the low emission zones observed by Viking in the thermal infrared (Fig. 19), including their temporal and spatial scales, their intensity, their latitudinal distribution and their sensitivity to the dustiness of the atmosphere (Forget et al. 1998b).

This new parameterization, used in combination with the DTM topography and with allowance for a varying atmospheric dust content, allows the GCM to simulate the CO_2 condensation-sublimation cycle realistically. In particular, the seasonal variations of the surface pressure recorded by the Viking Landers are reproduced without artificially decreasing the condensation rate as was done in previous studies (e.g. Hourdin et al. 1995, Pollack et al. 1993) by reducing the global emissivity of the caps.

References

Anderson, E. and Leovy, C. (1978). Mariner 9 television limb observations of dust and ice hazes on Mars. *J. Atmos. Sci.*, 35:723–734.

Baines, P. G. and Palmer, T. N. (1990). Rationale for a new physically-based parametrisation of sub-grid scale orographic effects. Technical Report 169, Eur. Cent. for Medium-Range Weather Forecasts, Reading, England.

Blackadar, A. K. (1962). The vertical distribution of wind and turbulent exchange in neutral atmosphere. *J. Geophys. Res.*, 67:3095–3102.

Clancy, R. T. and Lee, S. W. (1991). A new look at dust and clouds in the Mars atmosphere: Analysis of emission-phase function sequences from global Viking IRTM observations. *Icarus*, 93:135–158.

Clancy, R. T., Lee, S. W., Gladstone, G. R., McMillan, W. W., and Rousch, T. (1995). A new model for Mars atmospheric dust based upon analysis of ultraviolet through infrared observations from Mariner 9, Viking, and Phobos. *J. Geophys. Res.*, 100:5251–5263.

Collins, M., Lewis, S., and Read, P. L. (1997). Gravity wave drag in a global circulation model of the Martian atmosphere: parametrisation and validation. *Adv. Space Res.*, 44:1395–1409.

Conrath, B. J. (1975). Thermal structure of the Martian atmosphere during the dissipation of dust storm of 1971. *Icarus*, 24:36–46.

Davies, M. E., Batson, R. M., and Sherman, S. C. W. (1992). Geodesy and cartography of Mars. In *Mars*, pages 321–342. Univ. of Ariz. Press, Tucson.

Dufresne, J. L., Fournier, R., and Grandpeix, J. Y. (1998). The monte-carlo exchange method for radiative budget computation in a gas-filled two dimensional enclosure. *C. R. Acad. Sci. Série II b*, 326:33–38.

Eluszkiewicz, J. (1993). On the microphysical state of the Martian seasonal caps. *Icarus*, 103:43–48.

Forget, F. (1998). Improved optical properties of the Martian atmospheric dust for radiative transfer calculations in the infrared. *Geophys. Res. Lett.*, 25:1105–1109.

Forget, F., Hourdin, F., Fournier, R., Hourdin, C., Talagrand, O., Collins, M., Lewis, S. R., Read, P. L., and Huot., J.-P. (1999). Improved general circulation models of the Martian atmosphere from the surface to above 80 km. J.G.R., in press.

Forget, F., Hourdin, F., Hourdin, C., and Talagrand, O. (1998a). Simulation of dust lifting and transport with the LMD Mars general circulation model. *Bull. Am. Astron. Soc.*, 30:1023.

Forget, F., Hourdin, F., and Talagrand, O. (1998b). CO_2 snow fall on Mars: Simulation with a general circulation model. *Icarus*, 131:302–316.

Forget, F. and Pollack, J. (1996). Thermal infrared observations of the condensing Martian polar caps: CO_2 ice temperatures and radiative budget. *J. Geophys. Res.*, 101:16,865–16,880.

Forget, F., Pollack, J. B., and Hansen, G. B. (1995). Low brightness temperatures of Martian polar caps: CO_2 clouds or low surface emissivity? *J. Geophys. Res.*, 100:21,119–21,234.

Fouquart, Y. and Bonnel, B. (1980). Computations of solar heating of the Earth's atmosphere: A new parametrization. *Contrib. Atmos. Phys.*, 53:35–62.

Galperin, B. A., Kantha, L. H., Hassid, S., and Rosati, A. (1988). A quasi-equilibrium turbulent energy model for geophysical flows. *J. Atmos. Sci.*, 45:55–62.

Haberle, R., Houben, H. C., Hertenstein, R., and Herdtle, T. (1993). A boundary layer model for Mars: Comparison with Viking Lander and entry data. *J. Atmos. Sci.*, 50:1544–1559.

Haberle, R. M. and Jakosky, B. M. (1991). Atmospheric effects on the remote determination of thermal inertia of Mars. *Icarus*, 90:187–204.

Hansen, J. E. and Travis, L. D. (1974). Light scaterring in planetary atmosphere. *Space Sci. Rev.*, 16:527–610.

Helfand, H. M. and Labraga, J. C. (1988). Design of a nonsingular level 2.5 second-order closure for the prediction of atmospheric turbulence. *J. Atmos. Sci.*, 45:113–132.

Hoskins, B. J. and Simmons, A. J. (1975). A multi-layer spectral model and the semi-implicit method. *Q. J. R. Meteorol. Soc.*, 109:771–783.

Hourdin, F. (1992a). Conservation du moment angulaire dans le modèle de circulation générale du LMD. Note Interne 175, Lab. de Météorol Dyn., Cent. Nat. de la Rech. Sci., Paris.

Hourdin, F. (1992b). A new representation of the CO_2 15 μm band for a Martian general circulation model. *J. Geophys. Res.*, 97(E11):18,319–18,335.

Hourdin, F., Forget, F., and Talagrand, O. (1995). The sensitivity of the Martian surface pressure to various parameters: A comparison between numerical simulations and Viking observations. *J. Geophys. Res.*, 100:5501–5523.

Hourdin, F., Le Van, P., Forget, F., and Talagrand, O. (1993). Meteorological variability and the annual surface pressure cycle on Mars. *J. Atmos. Sci.*, 50:3625–3640.

Jacobsen, I. and Heise, E. (1982). A new economical method for the computation of the surface temperature in numerical models. *Contrib. Atmos. Phys.*, 55:128–141.

James, P. B., Kieffer, H. H., and Paige, D. A. (1992). The seasonal cycle of carbon dioxide on Mars. In *Mars*, pages pp. 934–968, Tucson. University of Arizona Press, Tucson.

Jaquin, F., Gierasch, P., and Kahn, R. (1986). The vertical structure of limb hazes in the Martian atmosphere. *Icarus*, 68:442–461.

Kieffer, H. H., Chase, S. C., Miner, E. D., Palluconi, F. D., Münch, G., Neugebauer, G., and Martin, T. Z. (1976). Infrared thermal mapping of the Martian surface and atmosphere: First results. *Science*, 193:780–786.

Kieffer, H. H., Martin, T. Z., Peterfreund, R., Jakosky, B. M., Miner, E. D., and Palluconi, F. D. (1977). Thermal and albedo mapping during the Viking primary mission. *J. Geophys. Res.*, 82:4249–4291.

Lewis, S. R., Collins, M., Read, P. L., Forget, F., Hourdin, F., Fournier, R., Hourdin, C., Talagrand, O., and Huot., J.-P. (1999). A climate database for Mars. Submitted to J.G.R.

Lindzen, R. S. (1981). Turbulence and stress owing to gravity wave and tidal breakdown. *J. Geophys. Res.*, 86:9707–9714.

Lopez-Puertas, M. and Lopez-Valverde, M. (1995). Radiative energy balance of CO_2 non-LTE infrared emissions in the Martian atmosphere. *Icarus*, 114:113–129.

Lott, F. and Miller, M. (1997). A new sub-grid scale orographic drag parametrization: its formulation and testing. *Q. J. R. Meteorol. Soc.*, 123:101–128.

MacVean, M. K. (1983). The effect of horizontal diffusion on baroclinic development in a spectral model. *Q. J. R. Meteorol. Soc.*, 38:771–783.

Markiewicz, W. J., Sablotny, R. M., Keller, H. U., Thomas, N., Titov, D., and Smith, P. H. (1999). Optical properties of the Martian aerosols as derived from imager for Mars Pathfinder midday sky brightness data. *J. Geophys. Res.*, 104:9009–9017.

Martin, T. Z. (1986). Thermal infrared opacity of the Mars atmosphere. *Icarus*, 66:2–21.

Martin, T. Z. and Richardson, M. I. (1993). New dust opacity mapping from Viking infrared thermal mapper data. *J. Geophys. Res.*, 98:10,941–10,949.

Mellor, G. L. and Yamada, T. (1982). Development of a turbulence closure model for geophysical fluid problems. *Rev. of Geophys.*, 20(4):851–875.

Miller, M. J., Palmer, P. M., and Swinbank, R. (1989). Parametrisation and influence of sub-grid scale orography in general circulation and numerical weather prediction models. *Meteorol. Atmos. Phys.*, 40:84–109.

Morcrette, J. J., Smith, L., and Fouquart, Y. (1986). Pressure and temperature dependence of the absorption in longwave radiation parametrizations. *Contrib. Atmos. Phys.*, 59(4):455–469.

Ockert-Bell, M. E., Bell III, J. F., McKay, C., Pollack, J., and Forget, F. (1997). Absorption and scattering properties of the Martian dust in the solar wavelengths. *J. Geophys. Res.*, 102:9039–9050.

Paige, D. A., Bachman, J. E., and Keegan, K. D. (1994). Thermal and albedo mapping of the polar regions of Mars using Viking thermal mapper observations, 1, North polar region. *J. Geophys. Res.*, 99:25959–25991.

Paige, D. A. and Keegan, K. D. (1994). Thermal and albedo mapping of the polar regions of Mars, 2, South polar region. *J. Geophys. Res.*, 99:25993–26013.

Palluconi, F. D. and Kieffer, H. H. (1981). Thermal inertia mapping of Mars from 60^{o}S to 60^{o}N. *Icarus*, 45:415–426.

Palmer, T. N., Shutts, G. J., and Swinbank, R. (1986). Alleviation of a systematic westerly bias in general circulation and numerical weather prediction models through an orographic gravity wave drag parametrisation. *Q. J. R. Meteorol. Soc.*, 112:1001–1039.

Phillips, S. P. (1984). Analytical surface pressure and drag for linear hydrostatic flow over three-dimensional elliptical mountains. *J. Atmos. Sci.*, 41:1073–1084.

Pierrehumbert, R. T. and Erlick, C. (1977). On the scattering-greenhouse effect of CO_2 ice clouds. J. Atmos. Sci, in press.

Pleskot, L. K. and Miner, E. D. (1982). Time variability of Martian bolometric albedo. *Icarus*, 50:259–287.

Pollack, J. B., Colburn, D. S., Flasar, F. M., Kahn, R., Carlston, C. E., and Pidek, D. (1979). Properties and effects of dust particles suspended in the Martian atmosphere. *J. Geophys. Res.*, 84(B6):2929–2945.

Pollack, J. B., Dalton, J. B., Grinspoon, D., Wattson, D. R. B., Freedman, R., and Crisp, D. (1993). Near-infrared light from Venus nightside: A spectroscopic analysis. *Icarus*, 103:1–42.

Pollack, J. B., Haberle, R. M., Schaeffer, J., and Lee, H. (1990). Simulations of the general circulation of the Martian atmosphere, 1, Polar processes. *J. Geophys. Res.*, 95:1447–1473.

Pollack, J. B., Ockert-Bell, M. E., and Shepard, M. K. (1995). Viking Lander image analysis of Martian atmospheric dust. *J. Geophys. Res.*, 100:5235–5250.

Rossow, W. B. (1978). Cloud microphysics: Analysis of the clouds of Earth, Venus, Mars, and Jupiter. *Icarus*, 36:1,50.

Roush, T., Pollack, J. B., and Orenberg, J. (1991). Derivation of midinfrared (5-25 μm) optical constants of some silicates and palagonite. *Icarus*, 94:191–208.

Sadourny, R. (1975). The dynamics of finite-difference models of the shallow-water equations. *J. Atmos. Sci.*, 32:680–689.

Sadourny, R. and Laval, K. (1984). January and July performance of the LMD general circulation model. In Berger, A. and Nicolis, C., editors, *New perspectives in Climate Modeling*, Elsevier, pages 173–197. Amsterdam.

Savijärvi, H. (1991). Radiative fluxes on a dust free Mars. *Contrib. Atmos. Phys.*, 2:103–112.

Seiff, A. (1982). Post-Viking models for the stucture of the summer atmosphere of Mars. *Adv. Space Res.*, 2:3–17.

Stansberry, J. A., Haberle, R. M., and McKay, C. P. (1995). Paper presented at the 27th Annual Meeting of the Division for Planetary Science of the AAS, Hawaii, October 9, 1995.

Toon, O. B., McKay, C. P., Ackerman, T. P., and Santhanam, K. (1989). Rapid calculation of radiative heating rates and photodissociation rates in inhomogeneous multiple scattering atmospheres. *J. Geophys. Res.*, 94:16,287–16,301.

Toon, O. B., Pollack, J. B., and Sagan, C. (1977). Physical properties of the particles composing the Martian dust storm of 1971-1972. *Icarus*, 30:663–696.

Warrilow, D. A., Sangster, A. B., and Slingo, A. (1986). Modeling of land surface processes and their influence on European climate. Technical Report DCTN 38, UKMO, Meteorological Office, London Road, Bracknell, Berkshire RG12 2SZ.

Washburn, E. (1948). *International critical tables of numerical data,physics, chemistry, and technology, volume 3*. New York: McGraw Hill.

Wood, S. E., Richardson, M. I., and Paige, D. A. (1996). A microphysical model of CO_2 snow on Mars. *Bull. Am. Astron. Soc.*, 28:1065.

Wu, S. S. C. (1978). Mars synthetic topographic mapping. *Icarus*, 33:417–440.

Wu, S. S. C. (1981). A method of defining topographic datums of planetary bodies. *Annales de Geophysique*, 1:147–160.

Zurek, R. W. (1982). Martian great dust storm, an update. *Icarus*, 50:288–310.

Zurek, R. W., Barnes, J. R., Haberle, R. M., Pollack, J. B., Tillman, J. E., and Leovy, C. B. (1992). Dynamics of the atmosphere of Mars. In *Mars*, pages 835–933. Univ. of Ariz. Press, Tucson.